Hydrodynamic interaction between coaxially rising bubbles in elastoviscoplastic materials: Equal bubbles

A. Kordalis, D. Pema, S. Androulakis, Y. Dimakopoulos, and J. Tsamopoulos*
Department of Chemical Engineering, University of Patras, Patras 26504, Greece

(Received 16 January 2023; accepted 12 July 2023; published 9 August 2023)

We consider the buoyancy-driven rise and interaction between two coaxially placed bubbles of equal size and constant volume that are initially stationary inside an elastoviscoplastic material. We simulate the material using the Saramito extension of the Herschel-Bulkley constitutive model, and we fit its properties to a 0.1% aqueous Carbopol solution. The interplay between plasticity, viscoelasticity, and inertia is investigated. We observe that a "bridge" of shear stresses develops, which connects the leading and the trailing bubble, decreasing the drag force on the latter and initiating their approach. The solidlike behavior of the material preserves stresses generated by the passage of the leading bubble and makes the material "softer" for the trailing bubble. At the same time the normal stresses primarily extend the bubbles, but their finite distance eventually causes the leading bubble to adopt a hydrodynamically less favorable shape that slows it down, further promoting the approach. Moreover, we examine the effect of the geometric characteristics and the material properties. Increasing the initial distance between the bubbles delays their approach, which, however, is inevitable. Increasing the radius results in a transition from the elastoplastic to a mixed elastoplastic-inertial regime and a delayed approach. Increasing elasticity or the shear and extension thinning of the material decreases the approach time. On the contrary, an increased viscosity delays their approach. Finally, varying the yield stress induces a nonmonotonic effect. Sufficiently small values of yield stress delay the approach compared to intermediate values, because it reduces the elastic response. Raising the yield stress slightly above the entrapment conditions of a single bubble, the bubbles still interact and move.

DOI: 10.1103/PhysRevFluids.8.083301

I. INTRODUCTION

Yield stress fluids are materials that have both solid and fluid response. Whether the former or the latter response is exhibited is determined by a property called yield stress. The significance of these materials lies in the plethora of industrial processes they are involved in and their daily applications. For instance, mayonnaise [1], hand gels [2], crude oil [3], and cement [4] are some prime examples of such fluids in the food, sanitary products, energy, and the construction industry, respectively, and have major financial impact. The dual nature of these materials, both solid and fluid, can lead to possible entrapment of bubbles existing in their bulk. In this scenario, the response of the material changes drastically, which is not necessarily a drawback. An example of a positive outcome is aerated chocolate. Entrapping bubbles in it improves its flavor and texture. However,

*tsamo@chemeng.upatras.gr

there are cases in which bubbles accidentally appear in the material and deteriorate its properties. For example, concrete honeycombing results from entrapped bubbles in cement, which decrease its mechanical strength. Therefore, it is essential to know how bubbles behave inside these complex materials.

Yield stress materials can be modeled in two distinct ways, depending on whether they exhibit elastic response or not. When elasticity is not accounted for, viscoplastic models result. There have been several numerical studies on a single bubble rising in viscoplastic materials [5–7]. However, as Kordalis *et al.* [8] pointed out, there is a controversial assumption in viscoplastic theory: the absolute rigidity of the solidlike region, which is also accompanied by numerical intricacies. When elastic effects are included, modeling is conducted using elastoviscoplastic (EVP) models. These models account for elasticity in both the solid and fluid regions. To our knowledge the only theoretical study on a rising single bubble inside an EVP material is by Moschopoulos *et al.* [9], which has nicely predicted earlier experimental observations [10,11]. Studies of single, rising bubbles in both viscoplastic and EVP materials have provided valuable information, and their comparison has resulted in useful conclusions regarding the role of elasticity. However, in all the examples presented in the beginning of our introduction, it would be unlikely to find just a single bubble rising with no interference from other bubbles forming a bubble swarm. This observation creates the incentive to study bubble interaction.

As Zhang *et al.* [12] mention in their extensive numerical study on interaction of bubbles inside Newtonian fluids, the microstructure of a buoyancy-driven suspension of bubbles is, to a large extent, governed by pair interactions. So studying the interaction between two bubbles provides valuable information also for the response in the presence of multiple bubbles. In non-Newtonian fluids there is a small number of numerical studies on the subject. Velez-Cordero *et al.* [13] studied the interaction of a pair of equal size bubbles positioned both in line and horizontally inside a shear thinning inelastic fluid. They observed that viscosity gradients play a crucial role in the approach of the bubbles. Recently two studies were published on the interaction in non-Newtonian fluids. The first one by Chaparian and Frigaard [14] examined multiple cylindrical air inclusions (circular bubbles solved in two dimensions) in a viscoplastic fluid. They investigated the effect of the volume fraction of air on the critical conditions for entrapment. They noticed that by increasing the volume fraction, the swarm of air inclusions could escape entrapment under conditions that a single air inclusion would have gotten entrapped. The second study is by Yuan *et al.* [15], who examined the interaction of bubbles placed in line with gravity in a viscoelastic shear thinning fluid for multiple combinations of bubble sizes. They observed that in bubble configurations with sizes below the critical value where velocity jump discontinuity occurs [16], a constant distance between the bubbles was achieved. To our knowledge, however, no study has focused on the interaction of a bubble pair inside yield stress materials accounting for their elastic behavior.

For this reason we examine the in-line configuration of bubbles rising inside an elastoviscoplastic material under the effect of buoyancy. The bubbles have the same volume, which remains constant throughout each simulation, given the short vertical distance traveled by the bubbles. First, we examine the mechanism of approach in the regime where elastoplastic phenomena are dominant. Then we evaluate the interplay between viscoelasticity, plasticity, and inertia by conducting an extensive parametric analysis varying initially the geometric characteristics of the flow, i.e., the initial separation distance between the bubbles and their radii. We continue by examining the effect of each material property of the surrounding fluid. Finally, we summarize our findings.

II. PROBLEM FORMULATION

We consider the buoyancy-driven rise of two equal-sized bubbles of constant volume V_b^*, positioned in line with the gravity field inside an unbounded EVP material, shown in Fig. 1. The quantities bearing the superscript * are dimensional, otherwise they are dimensionless. The bubbles have an initial separation distance d_o^* between their geometric centers. The material is incompressible with constant density ρ^*, elastic modulus G^*, consistency index k^*, shear-thinning

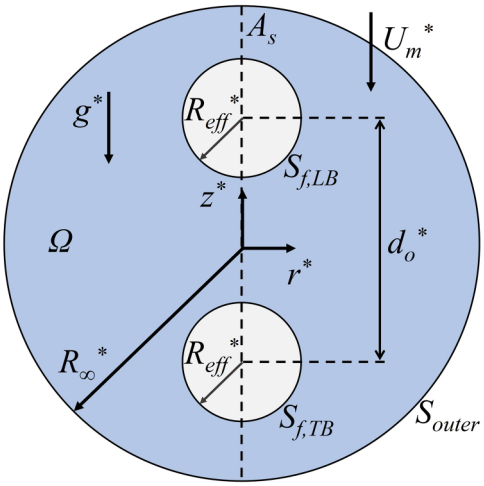

FIG. 1. Schematic representation of the two coaxial bubbles of equal size inside an elasto-visco-plastic material at the initial rest state. Ω denotes the volume of the EVP material, $S_{f,TB}$ and $S_{f,LB}$ the interfaces between air and material for the trailing bubble and leading bubble, respectively, and A_s and S_{outer} the symmetry axis and the outer boundary, respectively. The coordinate system is placed at the instantaneous middle of the distance between the bubble centers.

exponent n, and yield stress τ_y^*. We employ the Saramito extension of the Hershel-Bulkley (SHB) [17] constitutive model to capture the rheology of the material. The density and viscosity of the gas bubble are assumed to be negligible in comparison to the corresponding properties of the material. We also consider that the surface tension σ^* of the fluid-gas interface is constant in space and time. The bubbles are set free to move from rest under the effect of buoyancy. We adopt a cylindrical coordinate system with $\{r^*,\ z^*, \theta\}$ the radial, axial, and azimuthal coordinates, respectively, and assume axial symmetry. The center of the coordinate system is placed in the instantaneous middle of the distance between the two bubble centers and moves upwards with a distinct velocity U_m^*. The gravity vector points to the negative z direction. The bubble above the coordinate center will be referred to as the leading bubble (LB), and the bubble positioned below it as the trailing bubble (TB).

We scale all lengths with the effective radius, $R_{\text{eff}}^* = (3V_b^*/4\pi)^{1/3}$ of a spherical bubble with volume, V_b^*. We scale velocities by balancing buoyancy with inertial forces, i.e., $\sqrt{g^* R_{\text{eff}}^*}$, because this scaling of velocity is preferable as underlined by Moschopoulos *et al.* [9] and time with $\sqrt{R_{\text{eff}}^*/g^*}$. Pressure and stresses are scaled with $\rho^* g^* R_{\text{eff}}^*$. Consequently we arrive at the dimensionless numbers that govern this problem:

$$Ar = \frac{\rho^* g^* R_{\text{eff}}^*}{k^* \left(\frac{\sqrt{g^* R_{\text{eff}}^*}}{R_{\text{eff}}^*}\right)^n}, \quad Bn = \frac{\tau_y^*}{\rho^* g^* R_{\text{eff}}^*}, \quad Bo = \frac{\rho^* g^* R_{\text{eff}}^*}{\frac{\sigma^*}{R_{\text{eff}}^*}}, \quad Eg = \frac{\rho^* g^* R_{\text{eff}}^*}{G^*}. \tag{1}$$

Ar is the Archimedes number that balances buoyancy to viscous forces, Bn is the Bingham number that balances yield stress to buoyancy force, Bo is the Bond number that scales buoyancy to capillary forces. The last one, Eg, is the elastogravity number, which scales buoyancy force to elastic forces. Using the aforementioned nondimensionalization we arrive at the dimensionless forms of momentum and mass conservation equations:

$$\left(\frac{\partial \boldsymbol{u}}{\partial t} - \frac{dU_m}{dt}\boldsymbol{e}_z\right) + \boldsymbol{u}\cdot\nabla\boldsymbol{u} = \nabla\cdot\boldsymbol{T} - \boldsymbol{e}_z, \tag{2}$$

$$\nabla\cdot\boldsymbol{u} = 0, \tag{3}$$

where $\boldsymbol{T}$ is the Cauchy stress tensor split into pressure and extra stress $\boldsymbol{T} = -P\boldsymbol{I} + \boldsymbol{\tau}$. The fact that the coordinate system moves with the bubbles makes it noninertial and needs the extra term $\frac{dU_m}{dt}\boldsymbol{e}_z$. The datum pressure is set to zero at $z = 0$ on S_{outer}. When motion is initiated, the coordinate system translates upwards, following the bubbles, and the pressure at this point should be updated accordingly at each time step. In principle, this would affect the pressure in the bubble and, hence, its volume via, say, the ideal gas law, under isothermal conditions. Alternatively, a constant volume of bubbles can be retained, ignoring the small change in the datum pressure. We have examined both cases and concluded that under typical conditions in relevant experiments the difference in predictions is negligible. Thus, we follow the latter formalism. The extra stress tensor is related to the rate of strain, $\dot{\boldsymbol{\gamma}}$, according to the SHB model:

$$Eg\overset{\nabla}{\boldsymbol{\tau}} + \max\left[\text{Ar}(|\boldsymbol{\tau_d}| - \text{Bn}), 0\right]^{\frac{1}{n}} \frac{\boldsymbol{\tau}}{|\boldsymbol{\tau_d}|} = \dot{\boldsymbol{\gamma}}, \tag{4}$$

where $\boldsymbol{\tau}_d = \boldsymbol{\tau} - \text{tr}(\boldsymbol{\tau})/\text{tr}(\boldsymbol{I})$ is the deviatoric part of the stress tensor and $|\boldsymbol{\tau}_d| = \sqrt{0.5\boldsymbol{\tau}_d : \boldsymbol{\tau}_d}$ its magnitude. The max term in Eq. (4) introduces the von Mises criterion and dictates whether the material is yielded or not. When $|\boldsymbol{\tau}_d|$ is smaller than Bn the max term vanishes, and hyperelastic solid behavior is followed. Otherwise, the material flows. The yield surface, the interface between unyielded and yielded material, arises at $|\boldsymbol{\tau}_d| = \text{Bn}$. The upper-convected time derivative is defined as

$$\overset{\nabla}{\boldsymbol{\tau}} = \frac{\partial \boldsymbol{\tau}}{\partial t} + \boldsymbol{u}\cdot\boldsymbol{\nabla}\boldsymbol{\tau} - (\boldsymbol{\nabla}\boldsymbol{u})^T\cdot\boldsymbol{\tau} - \boldsymbol{\tau}\cdot\boldsymbol{\nabla}\boldsymbol{u}. \tag{5}$$

On the surface of each bubble a local force balance holds between the total stress tensor of the fluid, the pressure of each bubble and capillarity:

$$\boldsymbol{n_i}\cdot\boldsymbol{T} = P_{b,i}\boldsymbol{n_i} + B\text{o}^{-1}(2\mathcal{H}_i)\boldsymbol{n_i}, \quad \text{on} \quad S_{f,i} \quad \text{where} \quad i = LB,\ TB, \tag{6}$$

where $\boldsymbol{n_i}$ denotes the material-outward, unit, normal vector to the free surface of each bubble, $2\mathcal{H}_i = \boldsymbol{\nabla}_{\text{s}}\cdot\boldsymbol{n_i}$ is the mean curvature of a free surface with $\boldsymbol{\nabla}_{\text{s}} = (\boldsymbol{I} - \boldsymbol{nn})\cdot\boldsymbol{\nabla}$ the surface gradient operator, and $P_{b,i}$ is the pressure in bubble i. Also we impose the kinematic boundary condition on each bubble surface:

$$\boldsymbol{n_i}\cdot\left(\boldsymbol{u} - \frac{\partial \boldsymbol{r_f}}{\partial t}\right) = 0, \quad \text{on} \quad S_{f,i} \quad \text{where} \quad i = LB,\ TB, \tag{7}$$

where the derivative in (7) denotes the velocity of the mesh nodes in the fluid domain and $\boldsymbol{r_f}$ denotes the position vector of points on the free surface.

On the z axis we enforce symmetry conditions:

$$\boldsymbol{n_s}\cdot T\cdot\boldsymbol{t_s} = 0, \quad \text{on} \quad A_s, \tag{8}$$

$$\boldsymbol{n_s}\cdot\boldsymbol{u} = 0, \quad \text{on} \quad A_s, \tag{9}$$

where $\boldsymbol{n_s}, \boldsymbol{t_s}$ are the unit normal and unit tangent vectors to the axis, respectively. The outer boundary, located at $r = \sqrt{R_\infty - z}$, is far enough away from the center of the coordinate system, so that it does not affect the numerical results. In our simulations $R_\infty = 500$. At the outer boundary the material is certainly unyielded, which allows imposition of a uniform velocity,

$$\boldsymbol{u} = -U_m\boldsymbol{e_z}, \quad \text{on} \quad S_{\text{outer}}, \tag{10}$$

so that the center of the coordinate system becomes stationary in our calculations. Initially we assume the two bubbles to be spherical and the fluid to be at rest and stress-free:

$$\boldsymbol{u}(t=0) = \boldsymbol{\tau}(t=0) = \boldsymbol{0}. \tag{11}$$

Three extra variables arise: (1) the pressure of the LB, $P_{b,LB}$, (2) the pressure of the TB, $P_{b,TB}$, and (3) the rise velocity of the coordinate system U_m. To calculate each pressure, we constrain the

dimensionless volume of each bubble to be equal to $4\pi/3$ at all times. This volume is computed using

$$V_i = -\frac{1}{3}\int_{S_{f,i}} \boldsymbol{n_i}\cdot\boldsymbol{r_f}\, dS, \quad \text{where} \quad i = LB,\ TB. \tag{12}$$

The volume integral has been transformed into surface integral using the divergence theorem in Eq. (12). For the calculation of U_m, we impose that the coordinate system is always positioned at the middle between the centers of volume $z_{cv,i}$ of the bubbles:

$$z_{cv,LB} + z_{cv,TB} = \frac{3}{4}\frac{\int_{S_{f,LB}} z(\boldsymbol{n_{LB}}\cdot\boldsymbol{r_f})dS}{\int_{S_{f,LB}} \boldsymbol{n_{LB}}\cdot\boldsymbol{r_f}dS} + \frac{3}{4}\frac{\int_{S_{f,TB}} z(\boldsymbol{n_{TB}}\cdot\boldsymbol{r_f})dS}{\int_{S_{f,TB}} \boldsymbol{n_{TB}}\cdot\boldsymbol{r_f}dS} = 0. \tag{13}$$

Both volume integrals in Eq. (13) have been transformed again into surface integrals using the divergence theorem. After we solve the system of equations mentioned above at each time step, we can use the solution to calculate the drag force on each bubble according to

$$F_{d,i} = -\int_{S_{f,i}} \boldsymbol{e_z n_i} : (-\wp \boldsymbol{I} + \boldsymbol{\tau})dS\,, \quad \text{where} \quad i = LB,\ TB, \tag{14}$$

where $\boldsymbol{e_z}$ is the unit vector in the z direction and $\wp$ is the dynamic pressure, which is flow related only and defined as $\nabla\wp \equiv \nabla P + \boldsymbol{e_z}$.

III. NUMERICAL IMPLEMENTATION

These coupled equations are solved numerically using the Petrov-Galerkin stabilized Finite Element Method for Viscoelastic flows (PEGAFEM-V), as proposed by Varchanis *et al.* [18,19]. The novelty of this finite element formulation is the incorporation of equal order interpolants for all variables by extending the PSPG formulation [20]. This improves the stability of the numerical scheme with respect to mixed finite elements, while reducing the computational cost, the effort for code development, and the duration of simulations. DEVSS [21] is also used to maintain the elliptic nature of the momentum equation even when the Newtonian solvent is absent, which holds in our case. The hyperbolic character of the constitutive model is handled via the SUPG formulation [22]. The weak form of the momentum balance, continuity, and constitutive model along with the implementation of the free surface boundary conditions can be found in the work of Varchanis *et al.* [19]. The validity of the method has been tested thoroughly through several benchmarks, in which it exceeded previous high-Weissenberg number limitations, solve long-standing problems in viscoelastic flows, such as the sharkskin instability [23], and in more complex flows regarding elastoviscoplastic materials [8,9,24].

We approximate all variables with linear, three-node, Lagrangian basis functions. We employ the arbitrary Lagrangian-Eulerian (ALE) framework to track the liquid-air interface. We choose the elliptic grid scheme proposed by Dimakopoulos and Tsamopoulos [25] and extended by Chatzidai *et al.* [26] for the motion of the mesh nodes in the fluid domain. When the deformation of the mesh is large and the mesh quality drops below a limit, we remesh the domain and continue solving, as explained in the Appendix. The computational domain, prior to remeshing, is the initially undeformed one with the spherical bubbles. After each remeshing cycle, the computational domain changes to a new one based on the current location and shape of the bubbles.

We integrate in time using a fully implicit, second-order, backward finite difference scheme. At each new time step we use as an initial guess for the Newton algorithm the quadratic extrapolation of the previous solution. The time step is set to be constant throughout each simulation and equal to 0.02.

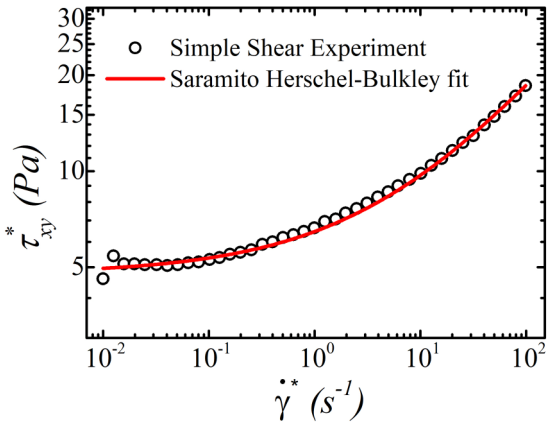

FIG. 2. Steady shear stress vs shear rate: experimental data (hollow symbols) and model predictions with the fitted parameters (red solid line).

IV. FLUID RHEOLOGY

We fit the SHB model to a 0.1% w/w Carbopol solution used in the work of Lopez *et al.* [10]. The elastic modulus G^* is acquired from the SAOS experiments they provide, while the other three properties, namely, the yield stress τ_y^*, consistency index k^*, and the HB exponent n, are derived by fitting the model to shear rheological data from their experimental study. In Fig. 2 we plot the experimental shear data and the fitting we obtained after determining these model parameters. The property values we extracted are given in Table I.

In Fig. 3 we show the model predictions of shear and extensional viscosity for simple shear flow and biaxial extension, as a function of the shear and extension rate, respectively. The extensional viscosity is defined as $\eta^*_{\text{ext}} = (\tau^*_{xx} - \tau^*_{yy})/\dot{\varepsilon}^*$. In both cases the material undergoes thinning, and its viscosity decreases as the respective deformation rate increases.

V. RESULTS AND DISCUSSION

We proceed with the analysis regarding the rise of the two equal-sized coaxially placed bubbles in EVP fluids. We examine the procedure of the bubble approach with buoyancy held constant and equal for both air inclusions throughout the phenomenon. We start our analysis with the underlying mechanism for the approach of the bubbles inside the EVP fluid for a representative case, which we call the "base case." Subsequently we perform a parametric analysis in two parts. The first part examines the effect of geometric characteristics: the initial separation distance d_o and the radii of the initially spherical bubbles R^*_{eff}, keeping the properties of the base material constant. The second part examines the effect of the material properties, by changing one property at a time from its value in the base material, keeping the initial separation distance and effective radius the same as that in the base case.

TABLE I. Values of the properties for the 0.1% Carbopol solution of Lopez *et al.* [10].

G^* (Pa)	τ_y^* (Pa)	k^* (Pa s^n)	n
40.42	4.8	1.75	0.47

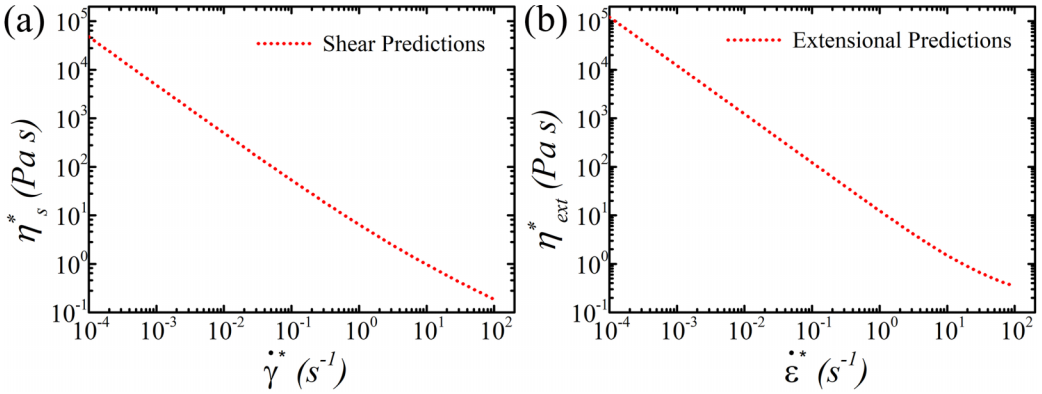

FIG. 3. Predictions of the SHB model for the viscosity in (a) simple shear and (b) biaxial stretch.

A. Base case

This section discusses bubbles of radius 4 mm in an initial separation distance of 20 mm inside the base material. The dynamics of the flow is investigated, focusing on the mechanism generating the approach of the bubbles when elastoplastic forces are dominant. The governing nondimensional numbers are $\mathrm{Ar} = 3.61$, $\mathrm{Bo} = 2.15$, $\mathrm{Eg} = 0.97$, and $\mathrm{Bn} = 0.12$. We observe a relatively large value of Bn if we consider that for a Herschel-Bulkley fluid with the same magnitude of Bo the limiting value for entrapment of a single bubble is around $\mathrm{Bn} = 0.14$ [6]. Hence, in the space of nondimensional numbers plasticity is important and elasticity is of the same order of magnitude as buoyancy. To draw conclusions from our results, we compare the predictions for the dual bubble configuration with the predictions for the single bubble rising under the same conditions. In this way we can separate the effects of the material nonlinear response from the bubble interaction that is taking place. We refer to the single bubble case as SB.

In Fig. 4 we show the time evolution of (a) the rise velocity, (b) the drag force, and (c) the aspect ratio defined as the largest height divided by the largest width of each bubble for LB, TB, and SB. We indicate key time instances with Latin numerals (i)–(vi) to explain the procedure of approach and show shapes of bubbles in Fig. 5, along with contours of shear stresses, normal axial stresses, and the yield surface.

Figure 4 shows that in the first selected instant (i), velocity, drag force, and aspect ratio for LB, TB and SB coincide. In Fig. 5 we see that the normal stresses and yield surfaces for LB and TB are identical, and both TB and LB behave just like SB. However, we also observe the formation of a "bridge" of shear stresses that extends from LB all the way back to TB. We should note that both shear and extensional stresses contribute to the yielding of the material. The axial normal stresses in the front pole of each bubble are negative meaning that the material is compressed, while the axial normal stresses at the rear pole of each bubble are positive, meaning that the material is stretched in that region. So, moving along the axis of symmetry starting from the rear pole of LB and arriving at the front pole of TB, the axial stresses are nullified somewhere in between, since their sign must change. If we define two auxiliary spherical coordinate systems originating at the centroid of each bubble, the large in absolute value contours of axial stresses are located in a polar angle (measured from the positive z axis) from 0° to 35° and from 145° to 180° approximately, as seen in Fig. 5(i). In the same contour plot, the shear stress values are dominant in a polar angle from 3° to 80° and from 100° to 187° This is precisely the reason why both bubbles have yielded regions in the union of polar angles mentioned earlier, i.e., from 0° to 80°, and from 100° to 180°, since both stress components contribute to the stress magnitude used in the von Mises criterion. Although close to each air-liquid interface axial stresses are large, away from it they fade rapidly. On the other hand, the shear stresses keep a rather small but nonzero value in a "bridge" connecting the bubbles. This

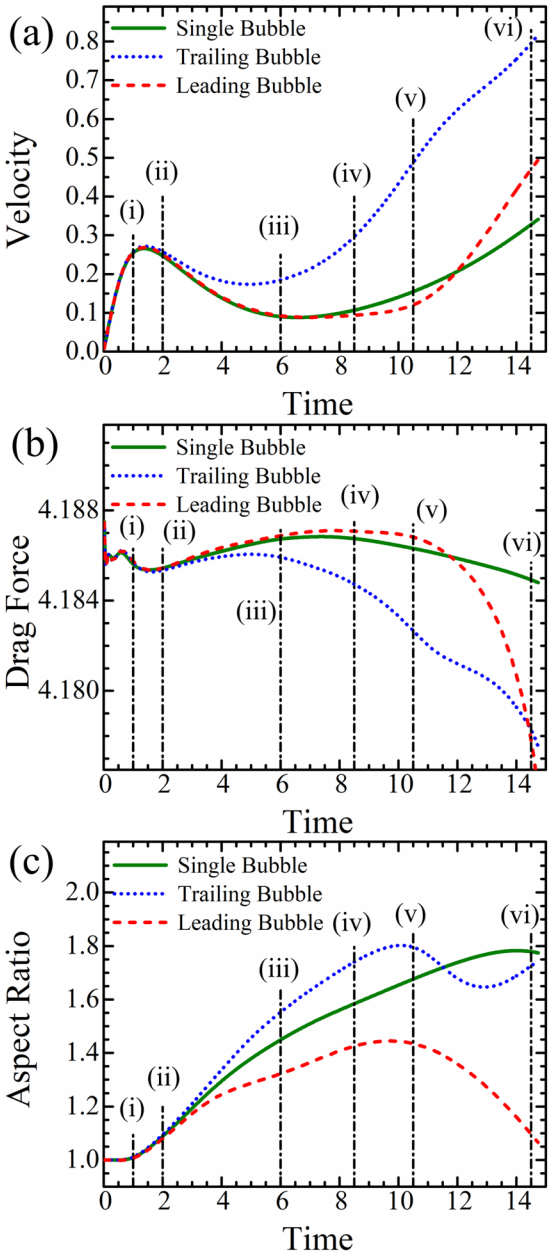

FIG. 4. Evolution of (a) velocity, (b) drag force, and (c) aspect ratio for SB, TB, and LB for the base case. Latin numerals indicate dimensionless time equal to (i) 1, (ii) 2, (iii) 6, (iv) 8.5, (v) 10.5, and (vi) 14.5, at which we will show bubble shapes, yield surfaces, and stress fields in Fig. 5.

contour formation loads material in front of TB with residual stresses, bringing it closer to yielding. These residual stresses remain inside the material indefinitely since there is no dissipation in the hyperelastic solid, as Syrakos *et al.* [27] point out in their study. This remark will prove quite handy in the following.

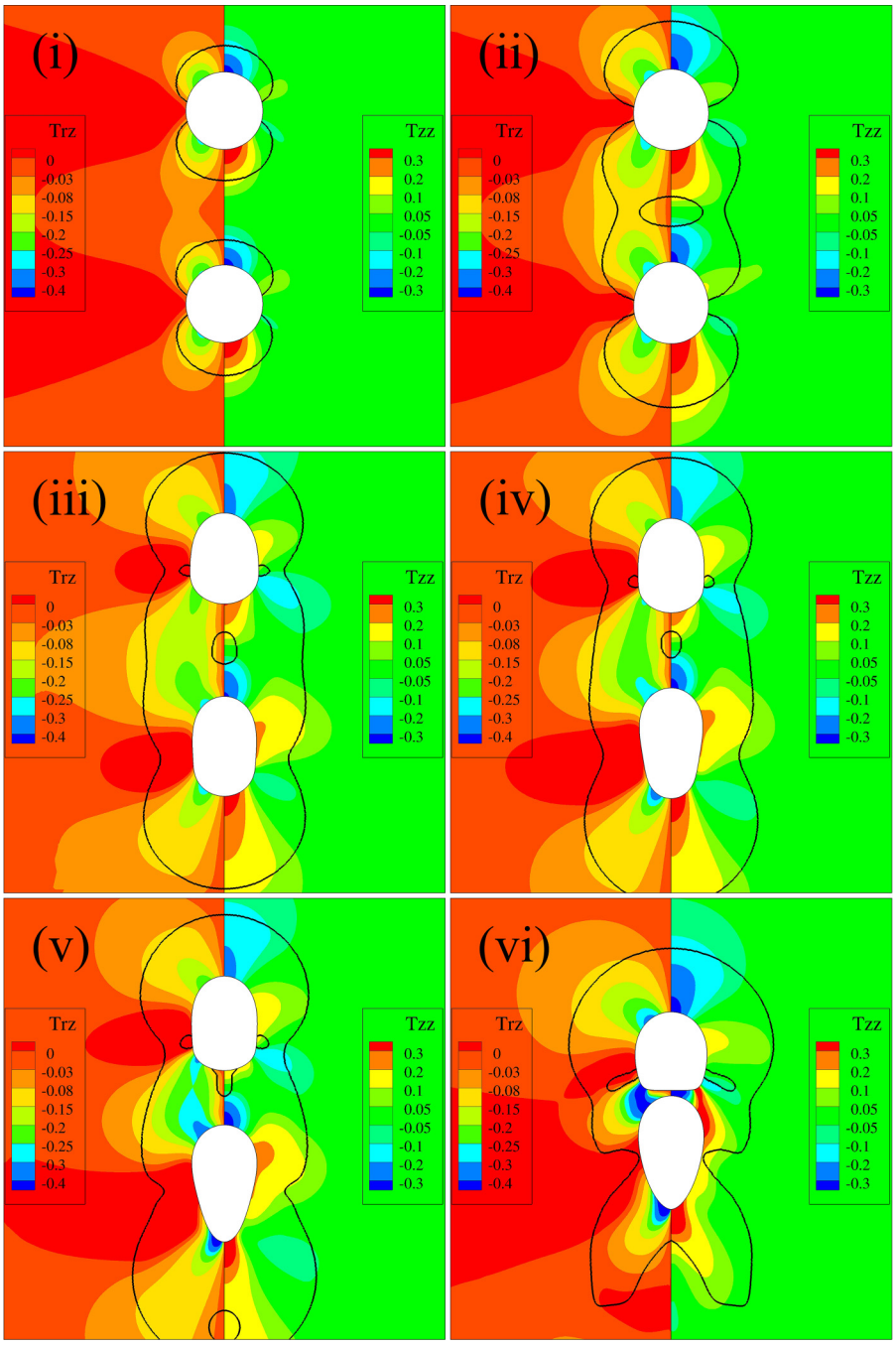

FIG. 5. Snapshots of the two bubbles in a sequence of time instances for the base case showing shear stresses to the left, normal axial stresses to the right, and the yield surface via a solid black line at times (i) 1, (ii) 2, (iii) 6, (iv) 8.5, (v) 10.5, and (vi) 14.5, indicated in Fig. 4.

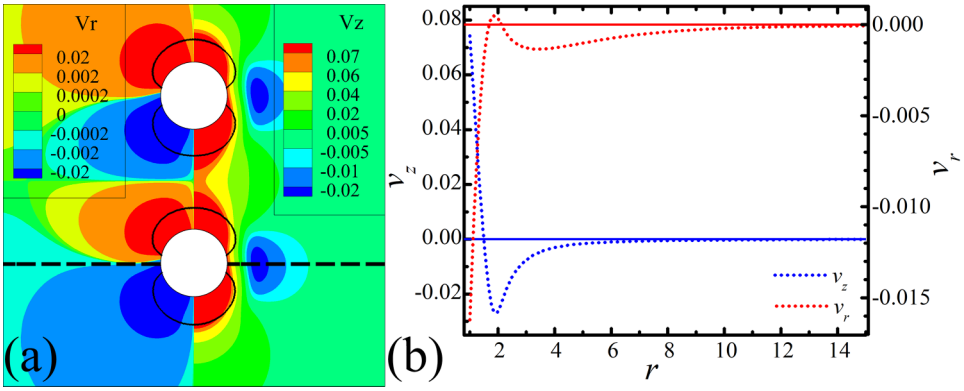

FIG. 6. At time instant (i) from Fig. 5, (a) contours of radial velocity to the left and axial velocity to the right and yield surface with black continuous lines, and (b) axial and radial velocities versus radial coordinate along the black dashed line to the side of the TB in (a).

An interesting observation is that in time instants (i) and (ii), the bubbles have a finite velocity, whereas unyielded material is in contact with them around the equatorial plane. In Fig. 6(a) we show the contours of radial velocity to the left and axial velocity to the right at time instant (i) of Fig. 5. The velocities are in an inertial frame where both bubbles travel upwards and the material in the far field is stationary. A black dashed line along the equatorial plane of the TB has been included. Along this line we depict the axial and radial velocities versus the radial coordinate in Fig. 6(b) and observe that both velocity components are nonzero close to the bubble, exhibit a local extremum due to elasticity, and finally drop to zero in the far field. Despite the fact that varying velocities lead to nonzero components of the deformation rate, the material along the dashed line remains unyielded. This is explained by examining the model for the unyielded part:

$$\overset{\triangledown}{\boldsymbol{\tau}} = \frac{\partial \boldsymbol{\tau}}{\partial t} = \frac{1}{Eg}\dot{\boldsymbol{\gamma}}. \tag{15}$$

Stresses increase with time, in the initially stress-free material due to the nonzero deformation rate, which inevitably is initially small. Only when the von Mises criterion is satisfied does the material yield. At (i) stresses have not built up yet. This explains the fading of the velocities to zero in the far field while at the same time the material remains unyielded. On the contrary, when a bubble rises in a viscoplastic fluid, the material cannot exhibit such behavior. Near the bubble, a finite deformation rate must exist, and the stresses increase abruptly. Hence, the material must be yielded there, and the velocity will drop to zero in the far field.

At time instant (ii), we observe that the yielded areas behind the leading bubble and in the front of the trailing bubble merge following the shear bridge contours, Fig. 5(ii). As we will discuss subsequently, this merging contributes to the interaction, but it does not necessarily declare its onset. At the same time an unyielded island remains in the middle. The reason is twofold: (1) the sign change in normal stresses mentioned earlier and (2) the small shear stresses close to the axis of symmetry that become precisely zero on the axis due to the imposition of symmetry conditions. Shortly after this time instant, in Fig. 4(b) the drag force of the TB decreases with respect to that in LB and SB that still coincide with each other. Consequently, the velocity of TB is increased in Fig. 4(a). The drop of the resistance to motion for the TB arises due to contact of the TB with material made "softer" by the passage of LB.

The effect of softened material has been shown in one of the experiments by Lopez *et al.* [10], where a bubble rising inside a yield stress material prefers to follow an inclined (with respect to gravity) path, instead of the usual vertical path. This was induced by loading the inclined path with residual stresses through the insertion and subsequent removal of a slender rod. In this specific

experiment, the flow is not axisymmetric, as opposed to our simulations, but exhibits the strong influence the residual stresses have on the reduction of resistance on a rising body. Apparently, in the rest of their experiments, bubbles rose vertically upward.

Moreover, the absence of dissipation in the hyperelastic solid gives rise to two distinct behaviors. The stresses in a previously yielded material that has been left to relax and decay asymptotically to the yield stress (or Bn in dimensionless form). The material close to the bubbles behaves accordingly. This behavior has been investigated and explained extensively by Syrakos *et al.* [27] in the lid-driven cavity of an EVP material. On the other hand, the stresses in a material that has remained unyielded from the beginning converge to a constant value below the yield stress. The material away from the bubbles behaves like that. Lopez *et al.* [10] mention that they waited at least 3 min before releasing a new bubble to avoid interaction between bubbles. This signifies that the timescale for dissipation in the solid phase is large compared to the time that the bubbles need to reach one another in our simulation. Therefore, the absence of dissipation in the unyielded material as predicted by the SHB model is acceptable according to the experiment.

At time instant (iii), the effect of the elastic normal stresses has become evident. In Fig. 5(iii) both bubbles have been deformed assuming prolate shapes. However, there is a difference with the isolated SB case. In Fig. 4(c) the aspect ratio of LB is less than the one of SB, while the aspect ratio of TB is larger than the one of SB. The reduced resistance on TB makes it easier to translate, while the open space behind its rear pole gives room for tensile stresses to develop spatially with no geometric restriction. This creates a larger aspect ratio with respect to SB and defines the onset for the creation of an inverted teardrop shape in TB, the drag force on which decreases and promotes its acceleration. We should also mention that after the encapsulation of both bubbles inside a single yielded envelope, additional mechanisms contribute to their approach. Shear and extension thinning come into effect. Velez-Cordero *et al.* [13] have reported that viscosity gradients draw bubbles closer in the shear thinning fluids they studied. Also, the pressure drop behind the rear pole of the LB draws the TB closer, a phenomenon called sheltering effect [12]. On the other hand, LB does not experience any reduction in its drag force while the distance from its rear pole to TB decreases. Tensile stresses do not extend to the same distance as in a SB, which leads the LB to take a less prolate shape.

At time instant (iv), the velocity of LB continues having an almost constant value, the same as in earlier times, while SB accelerates. Correspondingly, the drag force on LB is maintained at a constant high value. On the contrary, the drag force on SB is reduced. This contrast is again a product of the elastic stresses formed around the bubbles. The SB has developed the inverted teardrop shape. On the contrary, LB still has a prolate shape due to the confined space behind its rear pole, which decreases as bubbles approach each other. Interestingly, the shape resembles the case of a single bubble rising in viscoplastic fluid [5]. Also, the unyielded region at the side of LB seems fairly similar to the viscoplastic case. The difference is that LB does not have fore-aft symmetry with respect to its equatorial plane, and the small unyielded region in contact with it is not positioned on the equatorial plane as in the case of the bubble inside the viscoplastic material. Elasticity again creates this discrepancy. This prolonged shape with its side parallel to the z axis generates the highest resistance on LB, which is not attained by a single bubble in an unbounded medium under any circumstances.

At time instant (v), the unyielded island that used to be around the middle between the bubbles has now reached the rear pole of LB. So the magnitude of stresses in this region has dropped below the yield limit. Meanwhile in Fig. 4(c) both LB and TB exhibit the maximum value of their aspect ratio. This means that both bubbles start getting compressed after this time instant. Consequently, the swift motion of TB starts pushing the material in front of it, which in turn pushes LB. This is the reason why, despite its less favorable shape, LB experiences a drop in its drag force [Fig. 4(b)] and it begins accelerating [Fig. 4(a)]. It is obvious also from Fig. 4(a) that TB senses compression at its front and a slight drop in its acceleration when LB starts accelerating. After the maximum of aspect ratio, a global maximum to be precise, the aspect ratio of LB drops monotonically, while in the TB the global maximum is followed by a local minimum. So LB is elongated in the z direction

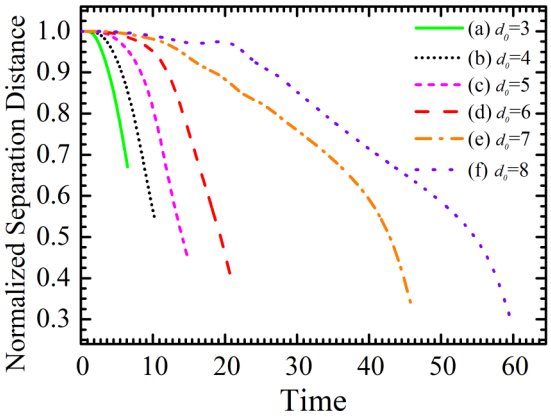

FIG. 7. Time evolution of normalized separation distance for all values of the initial separation distance with incubation times (a) 1.9, (b) 2.8, (c) 4, (d) 5.7, (e) 7.6, and (f) 9.5.

reaching an extremum and then it gets squeezed, while TB is elongated axially up to an extremum, then it gets squeezed and again elongated. This reelongation of TB appears because TB enters an area of significant pressure drop, and hence the sheltering effect becomes more pronounced.

Finally at time instant (vi), LB and TB have approached each other significantly, and the shape in the rear of LB has become flat. In Fig. 4(a) velocities of both LB and TB are higher than the SB velocity, and in Fig. 4(b) both drag forces are smaller than the SB drag force. Hence, the observation by Velez-Cordero *et al.* [13] that the mean drag experienced by each bubble is smaller than the drag on an isolated bubble of the same size also holds for yield-stress fluids with elasticity, due to their alignment, proximity, and close interaction in the direction of flow.

B. Effect of geometric characteristics

In this section we investigate the effect of geometric characteristics on the dynamics of the flow. Cases (a)–(f) of this section depict predictions when the initial separation distance is varied, while cases (g)–(n) predictions are when the radius of the bubbles is varied. Note that we omit numerals (i) and (l) on purpose to avoid confusion with indications of time instants used in the base case and similarity to the number one (1). The letter of each case is mentioned along with its dimensionless numbers.

1. Initial separation distance, d_o

We maintain the same material and size of bubbles used in the base case, so we have the same dimensionless numbers. Hence, we continue examining the bubble interaction in the elastoplastic regime. The initial separation distance cases covered in this section are (a) $d_o = 3$, (b) $d_o = 4$, (c) $d_o = 5$, (d) $d_o = 6$, (e) $d_o = 7$, and (f) $d_o = 8$. This translates to dimensional distances from 1.2 cm [case (a)] up to 3.2 cm [case (f)] between bubbles of 4 mm radii.

In Fig. 7 we plot the time evolution of the normalized separation distance, which is obtained by dividing its instantaneous value with the initial one for each case. Hence all curves start from unity. For an initial time period, which differs from case to case, the separation distance remains almost constant and equal to unity. During this incubation period both bubbles rise with nearly the same velocity as the SB and no interaction is observed. As expected, in this approach-only scenario, the cases with larger d_o have a longer incubation period. When the distance begins to decrease, the velocity of TB increases and interaction starts. To mark the onset of interaction we set a threshold of 1% drop in the separation distance from its initial value for each case. Irrespective of the initial

TABLE II. Geometrical characteristics and dimensionless numbers for all cases of different radius.

Case	R^*_{eff} (mm)	d^*_0 (mm)	Ar	Bo	Bn	Eg
(g)	3.5	17.5	3.06	1.65	0.139	0.85
(h) (Base case)	4.0	20.0	3.61	2.15	0.122	0.97
(j)	6.0	30.0	5.95	4.84	0.081	1.46
(k)	8.0	40.0	8.49	8.60	0.061	1.94
(m)	12.0	60.0	14.00	19.35	0.041	2.91
(n)	16.0	80.0	19.97	34.40	0.030	3.88

separation distance, we observe that equal-size bubbles approach each other. The bubble separation distance does not reach asymptotically a steady value.

In Fig. 8 we show the close-ups of bubble configurations at the onset of interaction. In Figs. 8(a)–8(d) the yielded areas of the two bubbles have already merged. On the contrary, in Figs. 8(e) and 8(f) the yielded areas are still separate from each other. Hence, merging of these areas does not constitute a necessary condition for the onset of interaction, since cases (e) and (f) do not satisfy it, but still the separation distance has decreased. In Fig. 8(a) the material behind the rear pole of LB is unyielded because extensional stresses are low locally. Based on our base case analysis, case (a) is already in the phase of TB thrusting LB. Also, the bubble shapes are nearly spherical, with LB being more compressed. In cases (b)–(d), the tensile stresses behind LB are larger and the unyielded island around the middle between bubbles appears and becomes larger with d_o. The bubble shapes become more prolonged with increasing d_o and more similar to each other. In cases (e) and (f) the shapes are even longer. In cases (e) and (f) there is no unyielded island but two separate yielded regions around the bubbles have formed. The shape of the LB in case (f) is comparable to the one of TB. For values of d_o even larger than those examined in this study, it seems that both shapes would coincide at the onset of interaction. Finally, the shear bridge is present in all values of d_o and promotes the approach in accordance with the base case.

The compressive stresses in front of LB and TB are different. This also holds for the tensile stresses at their rear poles. However, as d_o increases, the extensional stress contours become increasingly similar between LB and TB, with Fig. 8(f) presenting the stronger similarity. The feature that distinguishes the stored stresses in the material in front of the LB compared to the TB is introduced through the shear stress bridge. As we have already discussed, the latter loads the material with residual stresses that remain indefinitely. So the bubbles in all cases approach each other. Hence no stable chain configurations are observed similar to the ones in the work of Yuan *et al.* [15], who reported the formation of a stable chain (constant separation distance) for coaxial, equal-size bubbles of subcritical volume and rising in viscoelastic fluids. This difference is probably a consequence of the different rheological response under biaxial compression, which is extension thinning in soft jammed materials due to their bloblike structure [8], as opposed to extension hardening in viscoelastic fluids.

2. Radius, R^*_{eff}

We vary the radius of the bubbles, keeping them equal and examine their rise in the base material. We choose to fix the dimensionless initial separation distance in all cases. This gives the bubbles the same space relative to their size and allows for easier comparison of the results, although the dimensional separation distance changes. So we choose the constant $d_o = 5$ for all cases examined in this section. The different radii examined and the resulting values of the dimensionless numbers and of d^*_o are given in Table II.

In Fig. 9 we plot the dimensional separation distance versus dimensional time. We choose dimensional quantities in both axes because both the distance and time are made dimensionless using the radius. In this way results can be compared consistently. Starting with cases (g) and (h)

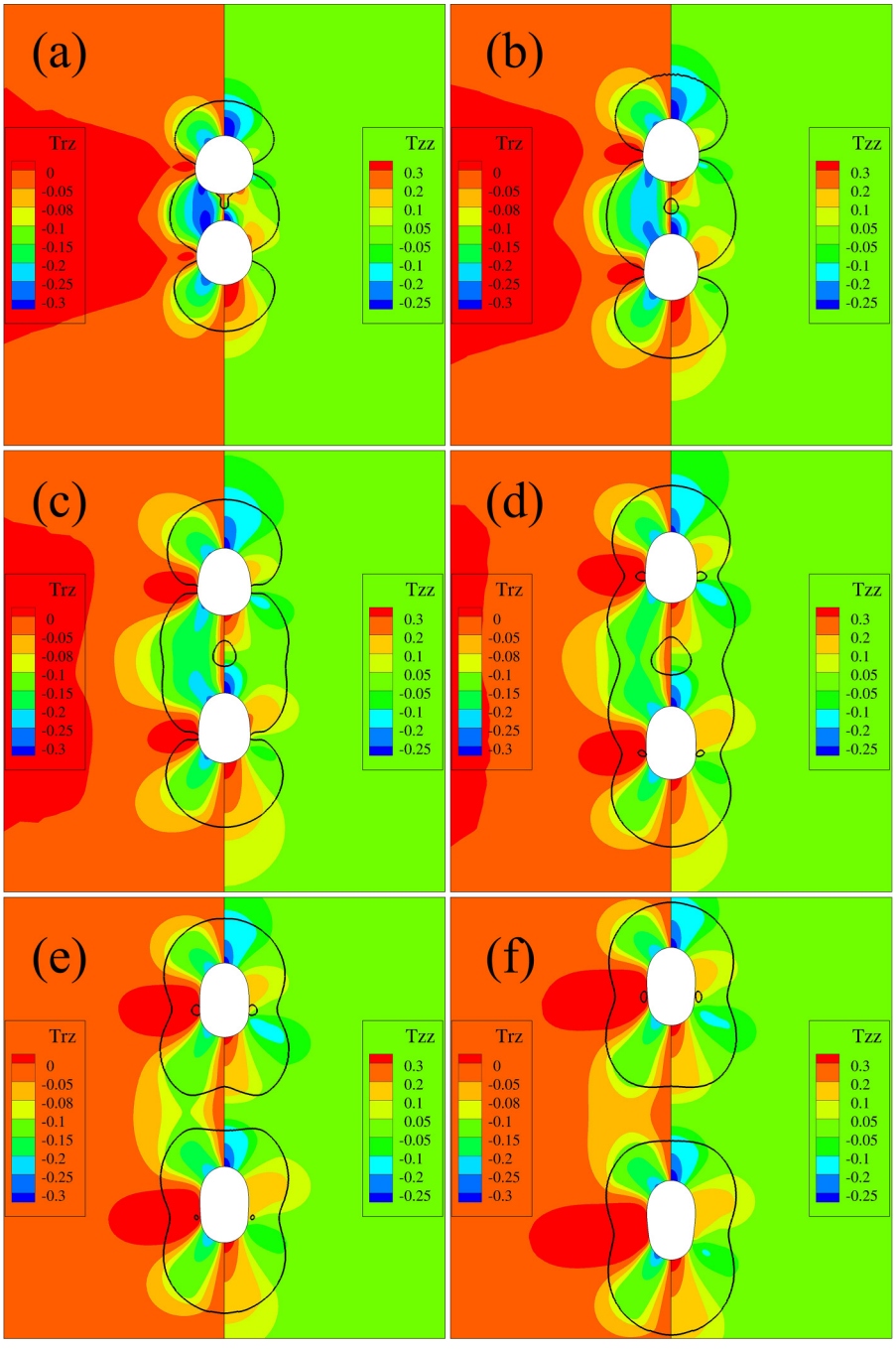

FIG. 8. Bubble configuration at the onset of interaction showing shear stresses to the left, normal axial stresses to the right and yield surface with solid black line for (a) $d_o = 3$ at time $= 1.9$, (b) $d_o = 4$ at time $= 2.8$, (c) $d_o = 5$ (base case) at time $= 4$, (d) $d_o = 6$ at time $= 5.7$, (e) $d_o = 7$ at time $= 7.6$, and (f) $d_o = 8$ at time $= 9.5$.

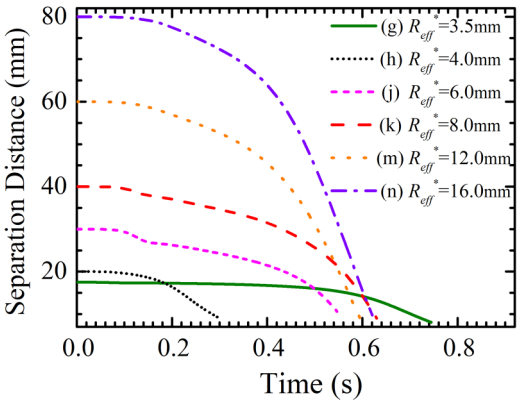

FIG. 9. Dimensional separation distance in mm vs dimensional time in seconds for all radii.

for 3.5 mm and 4 mm radius, respectively, in Fig. 9, we observe that (g) exhibits a very large plateau before the approach, while (h) shows a significantly smaller plateau. Note that case (g) has the largest Bn, close to 0.14, which is almost the entrapment condition of a SB in a viscoplastic fluid [6]. It is evident that plasticity dominates this case. On the other hand, case (h) has a mildly smaller value, close to 0.12, but the time of approach is significantly smaller. The initial separation distance is not very different between the two cases. It is useful to recall an observation by Moschopoulos *et al.* [9], who showed that the terminal rise velocity of a single bubble in an EVP material increases abruptly by increasing slightly the radius (or slightly decreasing Bn) for small bubbles in the elastoplastic regime. This observation is relevant in our comparison, because it underlines the differences induced in the intensity of the flow with small variations of the radius and consequently of Bn near the entrapment condition. Not only the intensity of the flow decreases, but also the time needed for a bubble to deform and translate in response to the forces acting on it and eventually to reach steady state increases. For this reason, the approach mechanism in near critical Bn conditions, with weaker stress fields, needs more time to surpass the yield limit set by the high Bn. Subsequently the approach mechanism is initiated.

Moving on to cases (j) and (k), we see an increase of the time of approach. First, the initial separation distance has increased notably by 10 mm to 30 mm with respect to the base case. Most importantly, however, the regime gradually changes from elastoplastic to inertial. This is revealed in Fig. 10 where we show the evolution of bubble shapes for radius 6 mm and 8 mm. Here the shapes change from inverted teardrops to nearly spherical and then oblate and the absolute value of slope of the bubble distance decreases in Fig. 9, case (j). This change prolongs the approach of the bubbles and introduces a dimple in the evolution of the bubble distance. The same transition is observed in case (k), although the change of slope is milder. However, its effect is pronounced as the total approach time for case (k) is even larger than for case (n) that has twice as large d_o^*. Basically, at early stages of motion the elastic normal stresses deform both LB and TB to inverted teardrop shapes. But then the velocities increase and enter a mixed elastoplastic-inertial regime, where elastic stresses are gradually suppressed, and shapes start becoming oblate.

An interesting observation is the resemblance between LB and TB shapes in Fig. 10, something that contrasts our observations in the base case. There TB has a hydrodynamically more favorable shape than LB, which contributes significantly to the drop of the drag force experienced by TB. Now that this contribution to the reduction of resistance is not present, the approach is based on the other mechanisms mentioned in the base case. The increase in contact time especially for case (k) underlines the significance of the TB's favorable shape and the role of elasticity to the approach. On the other hand, the dimensionless numbers in cases (m) and (n) indicate that inertial forces dominate. Hence, the shapes of TB and LB should become oblate immediately after motion starts. The suppression of elasticity as the radius is increased cannot be explained by the values of Eg alone,

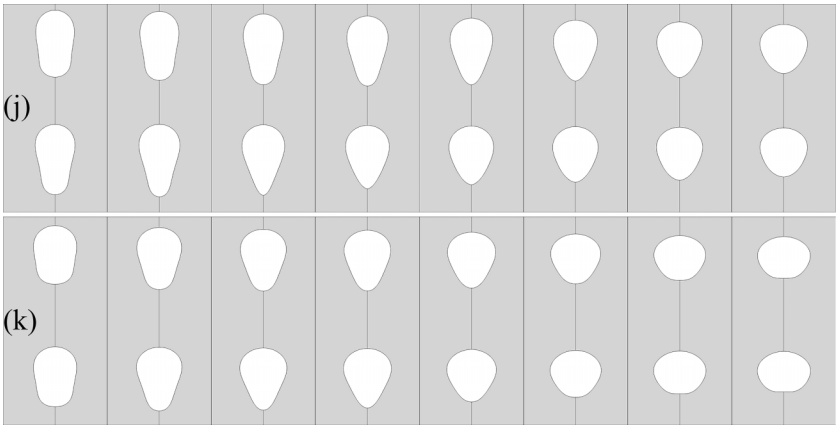

FIG. 10. Time evolution of cases (j) $R_{\text{eff}} = 6.0$ mm and (k) $R_{\text{eff}} = 8.0$ mm in the mixed elastoplastic-inertial regime.

because increasing the radius increases the elastogravity number also. As Moschopoulos *et al.* have pointed out [9], one should examine the auxiliary number, which is the product of relaxation time of the material and a characteristic strain rate. Thus, an increase in the radius decreases the Weissenberg number, Wi, defined as

$$Wi = \lambda \frac{\sqrt{g^* R^*_{\text{eff}}}}{R^*_{\text{eff}}} = \frac{\text{Eg}}{\text{Ar}}, \quad \text{where} \quad \lambda = \frac{k^* (\sqrt{g^*/R^*_{\text{eff}}})^{n-1}}{G^*}. \tag{16}$$

Finally, we present the bubble shapes for cases (g)–(n) right before the cessation of each simulation, when the thickness of the film between bubbles is equal to 0.15 along the axis. In Fig. 11 cases (g) and (h) seem almost identical. In case (j) we see the LB becoming more deformed creating room at its rear pole for the TB to fit. Its shape resembles inertial bubbles. The accompanying TB is slightly prolonged but with nearly fore-aft symmetry, being subjected to the two opposing forces, elastoplasticity trying to stretch it and inertia trying to compress it. Also, the yielded areas consist of two segments, one large, like an opened umbrella at the front, and a second less extended one in the back. In case (k) LB's deformation is the same as in case (j) but even more pronounced. TB has become oblate and the unyielded parts continue being separated with the front yielded umbrella becoming bigger. The corrugations of the yield surface of case (k) are explained in the Appendix. Finally in cases (m) and (n) the shapes are hatlike for both LB and TB, and the two yielded areas have grown further and merged. The constantly growing yielded areas are attributed to the considerable decrease of Bn, while the more deformed shapes to the significant increase in Bo and Ar. In the last four cases of Fig. 11, LB progressively engulfs more the TB, the fluid between them occupies a region of increasing extent, which is nowhere flat, and the distance between the two bubble perimeters does not vary too much. All these characteristics are in accordance with bubble shapes of tandem pairs observed in Newtonian liquids [28,29]. In the Appendix we show how the mesh is shaped for case (n) showed in Fig. 11.

C. Effect of material properties

In this section we investigate the effect of material properties on the dynamics of the flow. Cases (a)–(d) present the effect of elastic modulus, cases (e)–(h) the effect of consistency index, and cases (j)–(n) the effect of the shear-thinning exponent. Again, we omit numerals (i) and (l) for reasons explained earlier. Finally, cases (p)–(t) present the effect of yield stress; here we omit using numerals (o) and (r). The numeral of each case is mentioned in the respective subsection

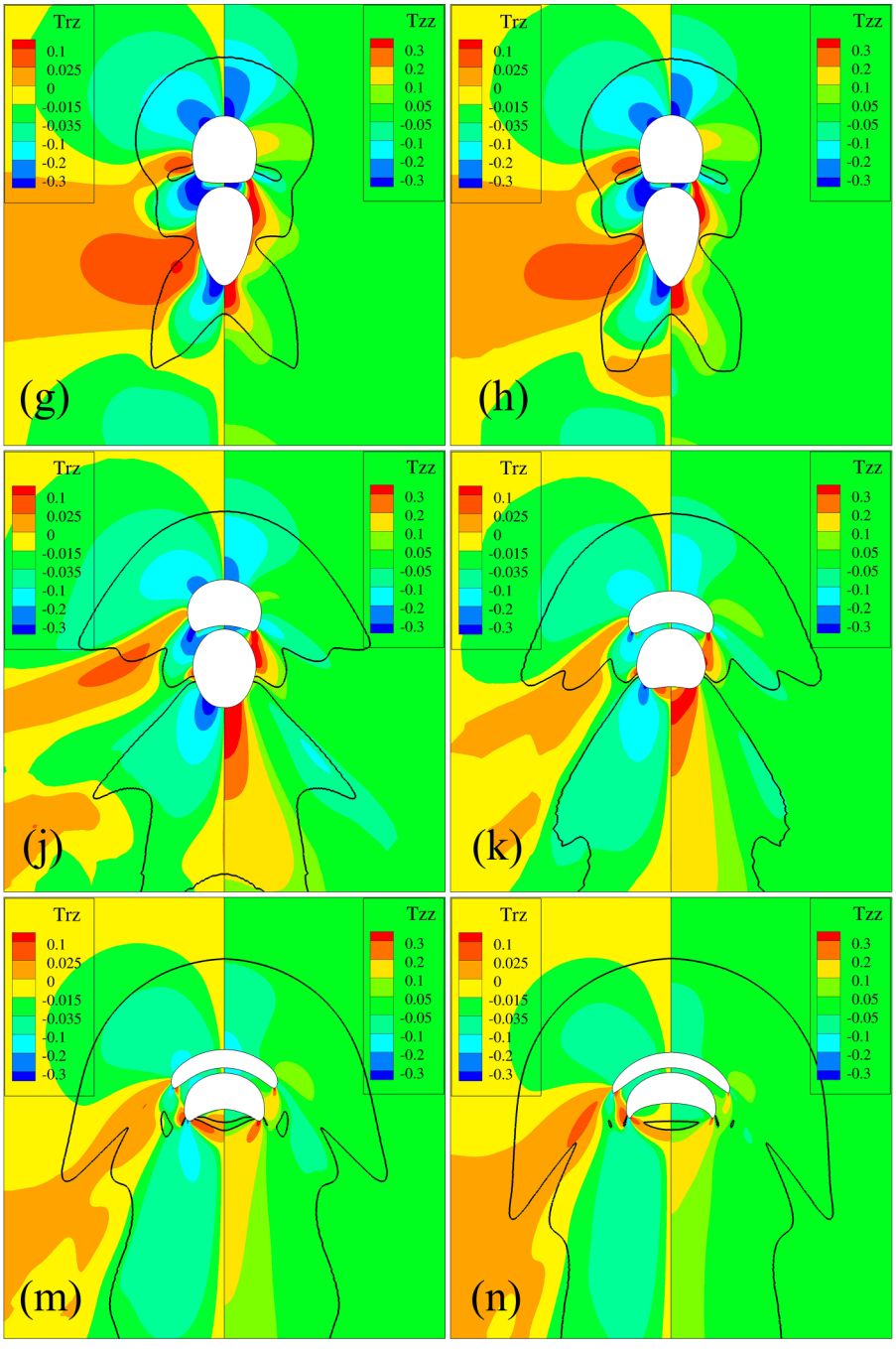

FIG. 11. Bubble configuration showing shear stresses to the left, normal axial stresses to the right and yield surface with solid black line before the end of each simulation for (g) $R^*_{\text{eff}} = 3.5$ mm, (h) $R^*_{\text{eff}} = 4$ mm, (j) $R^*_{\text{eff}} = 6$ mm, (k) $R^*_{\text{eff}} = 8$ mm, (m) $R^*_{\text{eff}} = 12$ mm, and (n) $R^*_{\text{eff}} = 16$ mm.

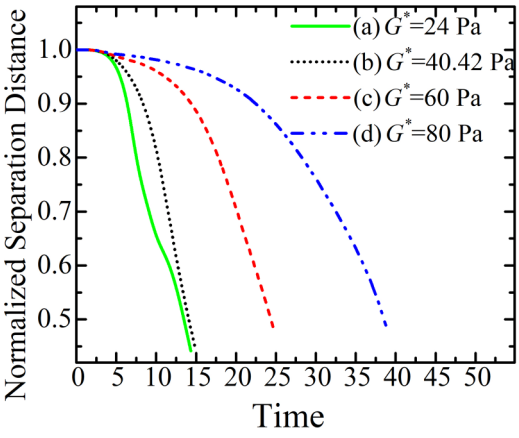

FIG. 12. Time evolution of normalized separation distance for the different values of the elastic modulus.

along with its dimensionless numbers. We choose to vary each property at a time instead of each dimensionless quantity because certain properties affect more than one dimensionless number and to a different extent. In all cases examined below, the size of the bubbles is $R^*_{\text{eff}} = 4$ mm and the initial dimensionless separation distance is $d_o = 5$.

*1. Elastic modulus, G**

In this subsection G^* assumes four values: (a) $G^* = 24$ Pa, (b) $G^* = 40.42$ Pa (Base case), (c) $G^* = 60$ Pa, and (d) $G^* = 80$ Pa. The elastic modulus affects only Eg. So equivalently this is a parametric analysis on Eg. The corresponding Eg values are (a) 1.63, (b) 0.97, (c) 0.65, and (d) 0.49. We depict our results in terms of G^*.

In Fig. 12 we plot the separation distance versus time for all G^*. Its evolution presents two stages: initially the distance decreases quite slowly in what we have called the incubation period, but subsequently much more rapidly, until the bubbles come close to each other. The materials with smaller values of G^* are more elastic, whereas the materials with larger values of G^* are more rigid. The very low G^* value of case (a) induces the fastest bubble approach, the smallest incubation period, and a more extended variation in the slope of the curve in its second stage, while raising G^* increases the approach time, and the incubation period, and decreases the absolute value of the nearly constant slope in each curve. All these signify that a more pronounced material elasticity alone accelerates the bubble approach.

In Fig. 13 we plot the velocity evolution. In all cases we see initially that the velocities of both LB and TB exhibit an elastic overshoot. The position of the overshoot is displaced to earlier times and its amplitude drops as we increase G^*. In all cases curves of TB and LB are superimposed until slightly after the overshoot, at time approximately 2, but then the TB velocity increases with respect to that of LB, which shows a small but steady drop followed by a plateau, Fig. 13(a). This plateau arises because the LB has a time lag in its deformation with respect to the TB. It acquires a prolate shape due to the confined space at its rear pole that is not so hydrodynamically favorable and results in a constant velocity, while TB accelerates. This favors the approach in all cases, but in lower values of G^*, TB moves much faster than LB and decreases their distance in shorter time. The value of the plateau also varies, exhibiting smaller velocities in larger values of G^*. We should note that case (a) shows a unique behavior. In cases (b)–(d) the prolate shape of the LB is formed and maintained up to the point that TB starts thrusting LB. In case (a) the stronger material elasticity overcomes the barrier of the confined space and manages to retain the inverted teardrop shape with a rounded rear part of LB, as shown in Fig. 14(a). This is seen clearly in Fig. 12, as variation of the slope and in Fig. 13(a) as the acceleration of LB in intermediate times. At time 11, we observe

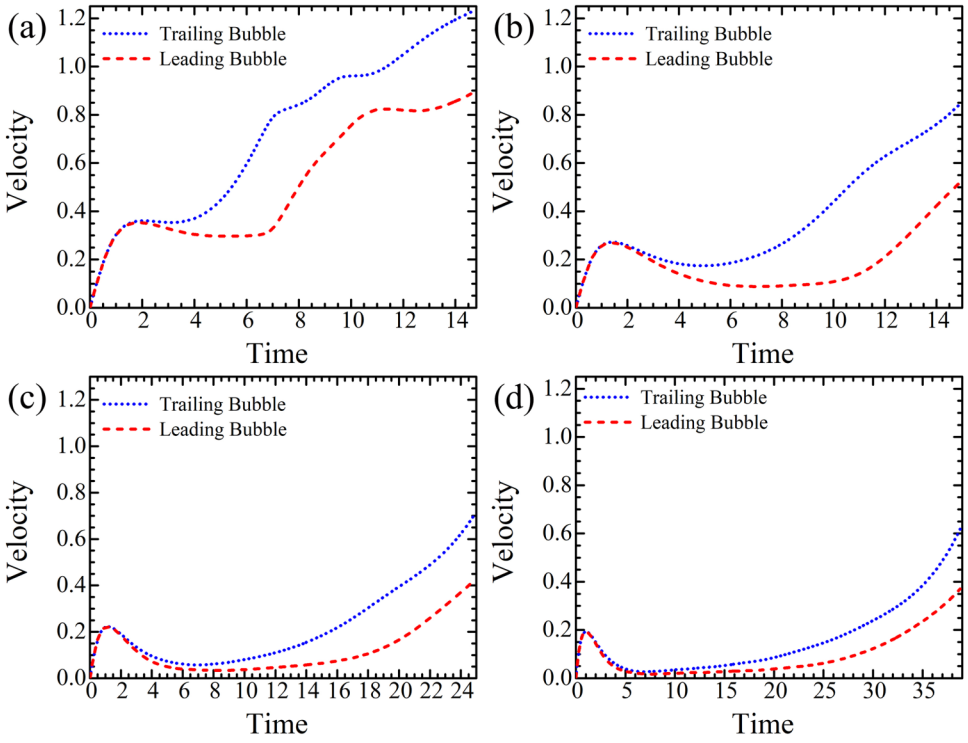

FIG. 13. Time evolution of bubble velocities for (a) $G^* = 24$ Pa, (b) $G^* = 40.42$, (base case), (c) $G^* = 60$ Pa, (d) $G^* = 80$ Pa.

that a second plateau is formed. This is the outcome of the confined space that eventually affects the shape of LB, decreasing its aspect ratio. At even larger times TB thrusts LB, making it accelerate.

In Fig. 14 we depict the effect of the elastic modulus on the bubble shapes, yield surface, and stress fields at the same bubble distance. First, in case (a) we see the inverted teardrop shapes for both TB and LB. This is the only case we have encountered where LB adopts and maintains this shape. The fact that both bubbles have hydrodynamically favorable shapes could create the anticipation that the approach would be delayed. Indeed, after both LB and TB assume teardrop shapes, they travel with a smaller difference in velocities, and the approach is delayed. This is shown in Fig. 12 for $G^* = 24$ Pa as the slope of the normalized separation distance drops its absolute value. In cases (b)–(d) the elastic effect gradually fades away, and TB becomes more and more prolate, resembling the shape formed in viscoplastic fluids. Another interesting observation is the size of the yielded areas around the bubbles. In $G^* = 24$ Pa the areas are smaller, and the shape of the yield surface of LB resembles the one for a SB. The yielded areas increase as we increase the elastic modulus. To explain this observation we need to introduce a new auxiliary dimensionless number, as pointed out by Kordalis *et al.* [8], the yield strain ϵ_y, defined as

$$\epsilon_y = \frac{\tau_y}{G} = BnEg. \tag{17}$$

The yield strain is the ratio of yield stress to the elastic modulus and measures the maximum strain a material can undergo before yielding. The lower the elastic modulus is, the higher the yield strain becomes (for constant yield stress). So the material in case (a) can undertake larger deformations before yielding and hence the yielded areas are smaller. On the other hand, the larger the elastic modulus becomes, the lower the yield strain is. The material becomes more brittle and breaks under smaller deformations, hence the larger yielded areas.

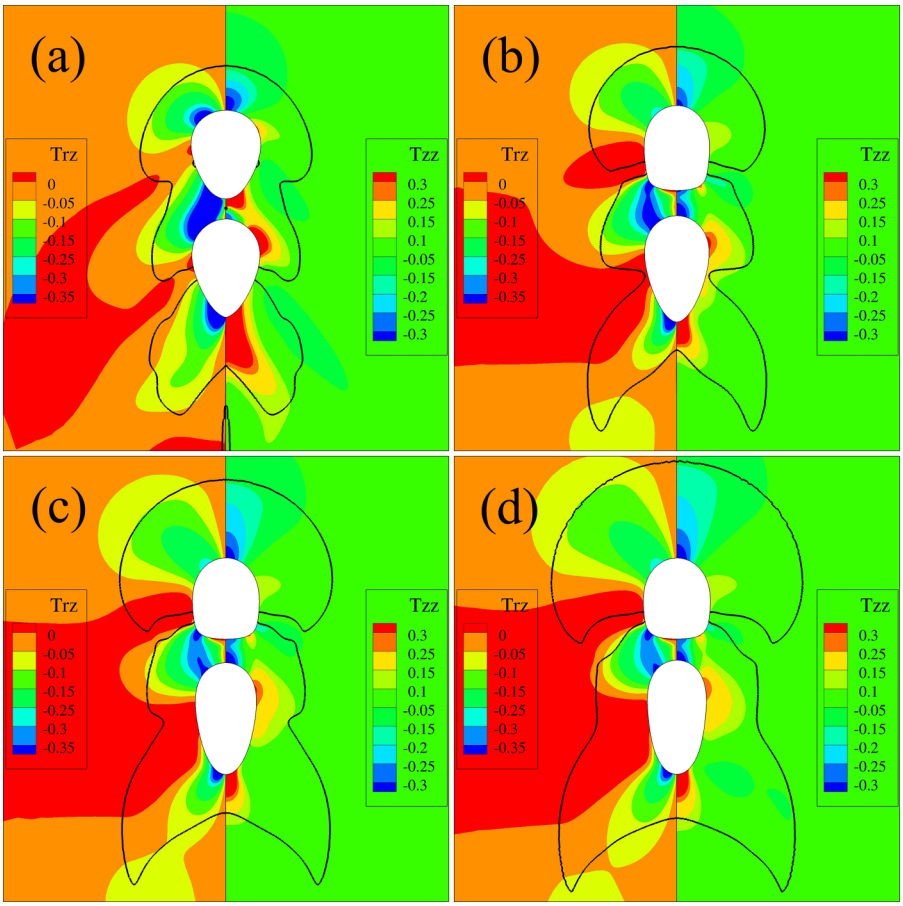

FIG. 14. Bubble shapes, yield surfaces indicated with a solid black line, shear stresses to the left, normal axial stresses to the right at normalized bubble distance 0.6 for (a) $G^* = 24$ Pa at time $= 10.5$, (b) $G^* = 40.42$ (base case) at time $= 12.5$, (c) $G^* = 60$ Pa at time $= 22$, and (d) $G^* = 80$ Pa at time $= 36.5$.

*2. Consistency index, k**

In this subsection k^* assumes four different values: (e) $k^* = 0.5$ Pa s^n, (f) $k^* = 1.75$ Pa s^n (base case), (g) $k^* = 2.5$ Pa s^n, and (h) $k^* = 3.5$ Pa s^n. The consistency index affects Ar. However, variation of Ar induces changes in the elastic response through the auxiliary Wi, which is inversely proportional to Ar. The corresponding Ar and Wi numbers are (e) 12.64 and 0.077, (f) 3.61 and 0.269, (g) 2.52 and 0.384, and (h) 1.8 and 0.538, respectively. We describe our results in terms of the consistency index k^*.

In Fig. 15 all evolution curves include the same two stages as in Fig. 12: the first one is an incubation period, which is followed by a much more rapid approach of the bubbles. The larger the value of k^*, the longer it takes for the bubbles to approach each other. Increasing the value of k^* increases the viscous resistance to flow of the material, but also increases Wi and, hence material elasticity, which reduces the approach time, as discussed earlier. Apparently, the viscous effects prevail, and they slow down the process, as k^* increases.

In Fig. 16 we plot the corresponding velocities. In cases (f)–(h) we can distinguish the velocity overshoot. On the contrary in case (e), there is no overshoot because the elastic phenomena have been suppressed significantly by the decrease of Wi by almost one order of magnitude compared to the other cases. Instead of a velocity plateau there is a continuous acceleration of varying magnitude.

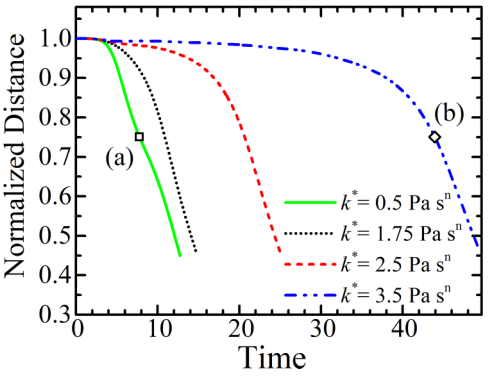

FIG. 15. Time evolution of normalized separation distance for the different values of the consistency index.

The large inertia (Ar = 12.64) prevents the formation of the high-resistance, prolate shape observed in the base case. In cases (f)–(h), an increase in k^* results in a decrease of the TB velocity and in a plateau in the LB velocity primarily. For example, in case (g) the velocity of TB starts diverging from the one of LB at time = 8, while at case (h) at time = 25. The plateau lasts longer, and the velocity is smaller, as k^* increases implying that the bubble deceleration is more pronounced after the overshoot.

Starting with case (e) in Fig. 17, the stresses are lower than in any other of the four cases in this comparison. The lower value of k^* creates mixed elastoplastic-inertial shapes similar to case

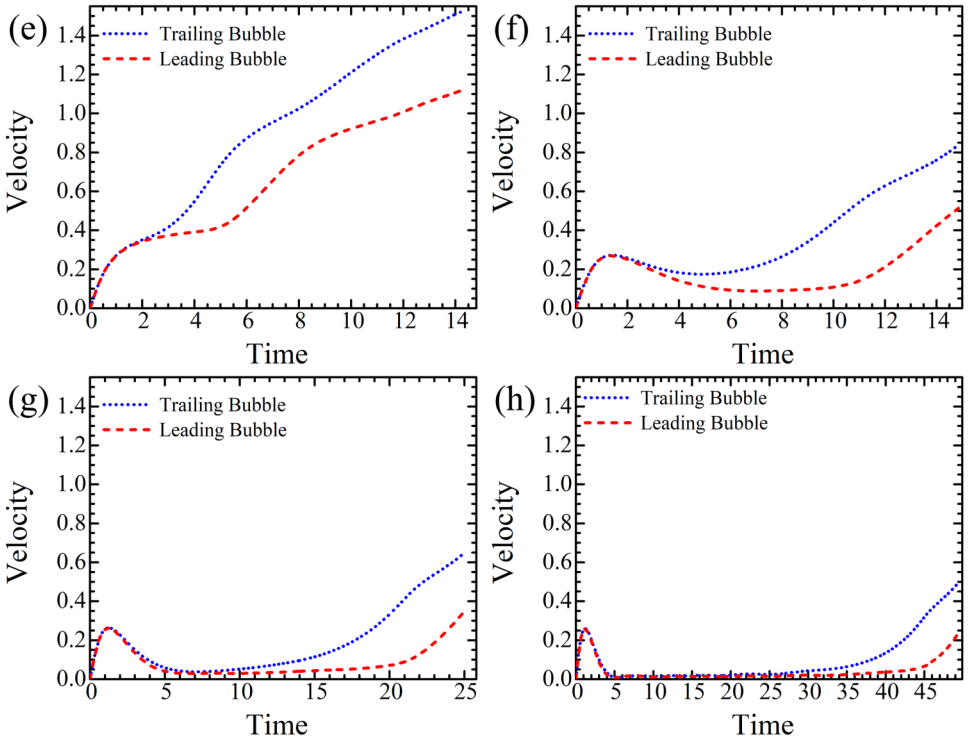

FIG. 16. Time evolution of bubble velocities for (e) $k^* = 0.5$ Pa s^n, (f) $k^* = 1.75$ Pa s^n (base case), (g) $k^* = 2.5$ Pa s^n, and (h) $k^* = 3.5$ Pa s^n.

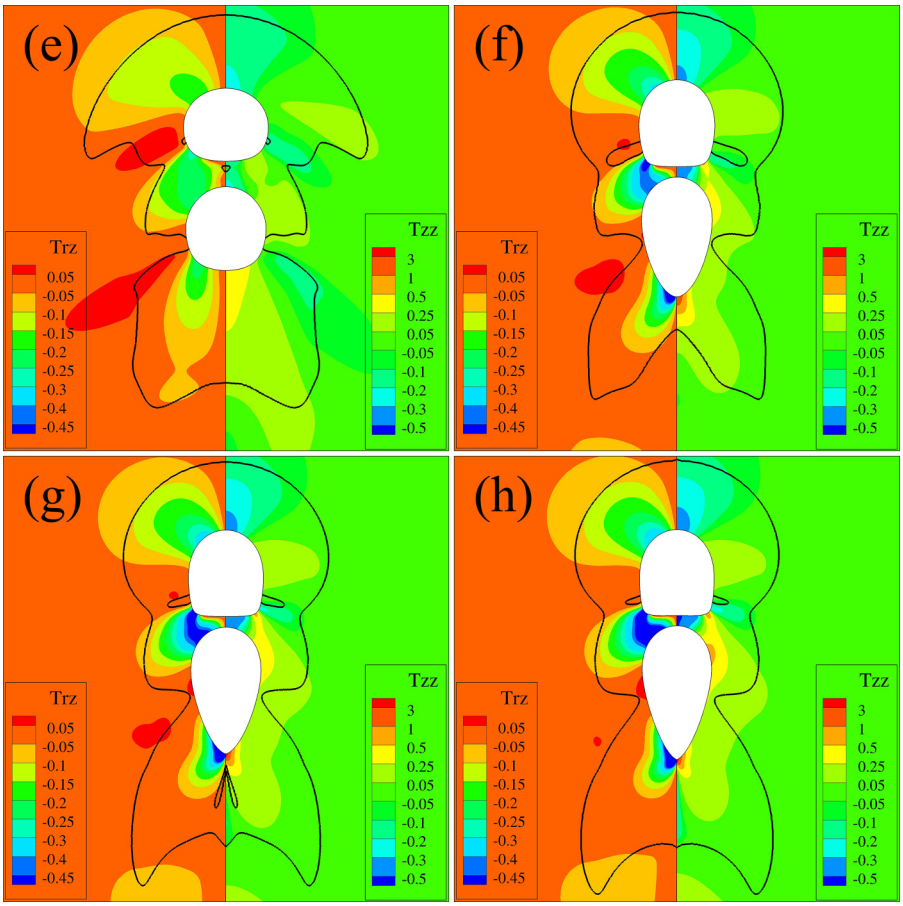

FIG. 17. Bubble shapes, shear stresses to the left, normal axial stresses to the right, and yield surface indicated by a solid black line at normalized separation distance 0.5 for (e) $k^* = 0.5$ Pa s^n at time = 12, (f) $k^* = 1.75$ Pa s^n (base case) at time = 14, (g) $k^* = 2.5$ Pa s^n at time = 24, and (h) $k^* = 3.5$ Pa s^n at time = 49.

(j). No large extensional stresses are observed. After the material yields and the bubble approach is initiated, the bubbles move easier in the less viscous medium. Also, the yielded area in the front assumes the same umbrella shape. The major difference between case (e) and case (j) is that case (e) has a lower Bo that makes the shapes less deformable. As we elevate the value of the consistency index, we notice that the stresses increase, and the shape of LB becomes flatter at its rear pole. The inverted teardrop shape in TB is present in cases (f)–(h) and becomes more pronounced with an increasing aspect ratio. The yield surfaces are not affected considerably in the three cases with larger k^*.

3. Power-law exponent, n

We discuss the following four values of n: (j) $n = 0.2$, (k) $n = 0.3$, (m) $n = 0.4$, and (n) $n = 0.47$ (Base case). The shear thinning exponent regulates the level of shear and extension thinning of the material. As we mentioned in the rheology section, EVP materials lack the material structure to exhibit extension rate hardening, and rarely does n assume values larger than 0.5 [8]. The power-law exponent affects Ar and consequently the auxiliary Wi number. Their corresponding values are (j)

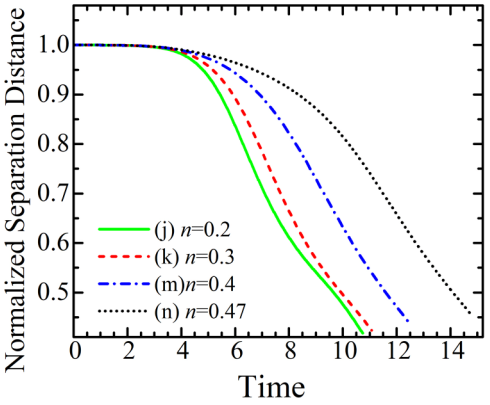

FIG. 18. Time evolution of normalized separation distance for all values of flow index.

10.27 and 0.094, (k) 6.95 and 0.14, (m) 4.71 and 0.21, and (n) 3.61 and 0.27, respectively. We present our results in terms of n.

In Fig. 18 we observe that a larger value of the HB exponent increases the approach time. The material becomes less shear thinning but more importantly less extension thinning, so its shear and extensional viscosity decrease less intensely. The incubation period is not affected significantly by n.

In Fig. 19 we show the evolution of bubble velocities. The higher the value of n is, cases (m) and (n), the larger the drop in the velocity of LB is after the overshoot and the bigger the extent of the

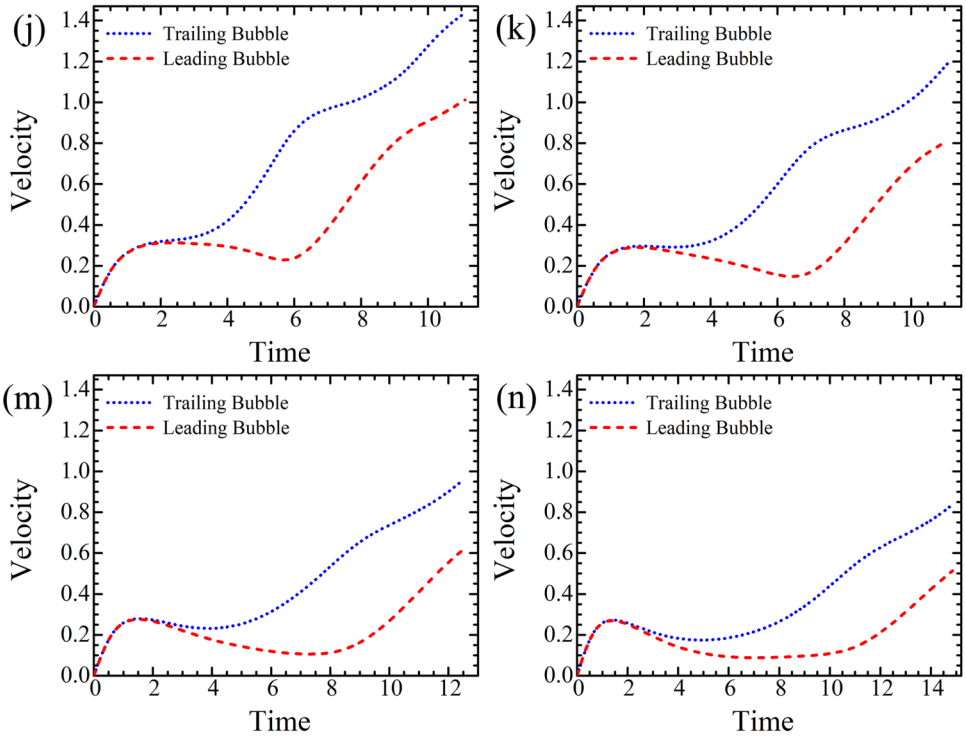

FIG. 19. Time evolution of bubble velocities for (j) $n = 0.2$, (k) $n = 0.3$, (m) $n = 0.4$, (n) $n = 0.47$ (base case).

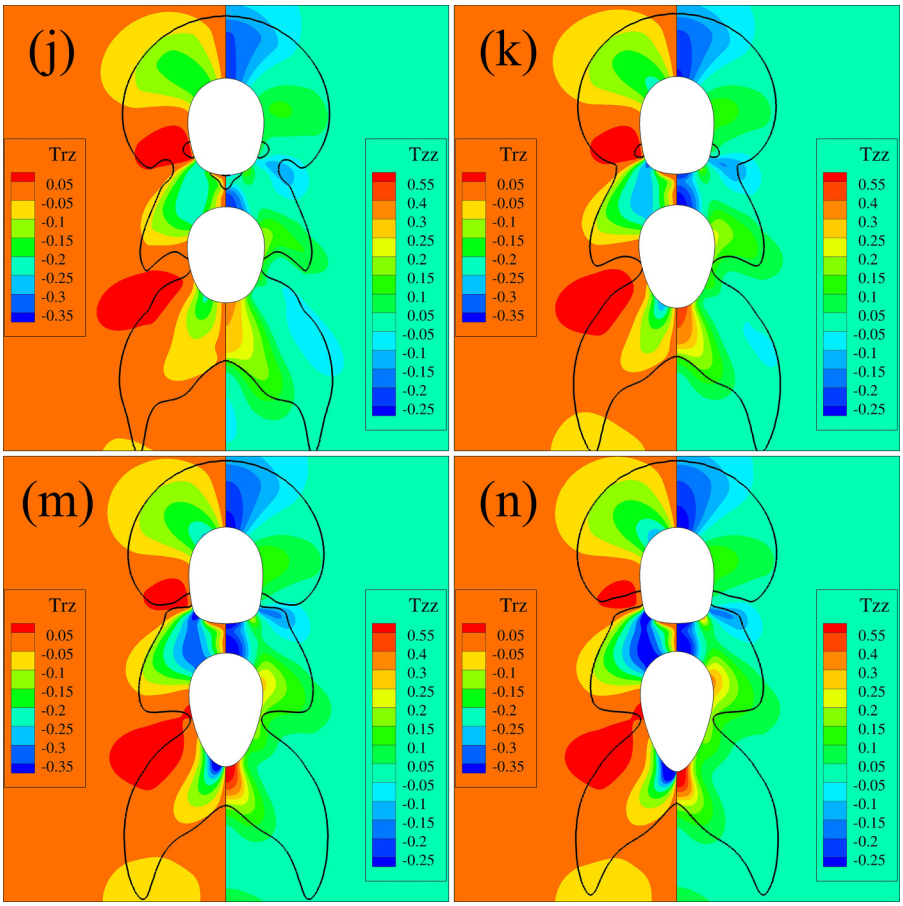

FIG. 20. Bubble shapes, shear stresses to the left, normal axial stresses to the right, and yield surface indicated by a solid black line at normalized separation distance 0.6 for (j) $n = 0.2$ at time $= 8$, (k) $n = 0.3$ at time $= 8.5$, (m) $n = 0.4$ at time $= 10.5$, and (n) $n = 0.47$ at time $= 13$ (base case).

plateau is. In these two cases also the velocity of TB has an overshoot. At lower values of n, cases (j) and (k), TB does not decelerate so there is no overshoot. The shear and extension thinning of the material create more intense viscosity gradients [13] in front of the TB that drop the resistance to flow. The velocity of LB also changes considerably exhibiting a smooth drop after the overshoot and a sharp increase afterwards. The less hydrodynamically favorable shape is created at earlier times, producing the smooth drop, but then the thrust by TB is felt and acceleration begins. The smaller the value of the flow index is, the earlier TB catches up with LB and starts pushing it.

In Fig. 20(j) we see that the bubbles are less prolonged in comparison with the other three cases due to higher Ar and consequently lower Wi. Raising n results in more deformed shapes axially, so that in cases (m) and (n) bubbles appear with the inverted teardrop shape. The stresses in case (j) have lower values, even though the bubble velocities are higher and decrease faster away from the bubbles due to the more intense shear and extension thinning of the material. The yield surfaces do not change appreciably.

4. Yield stress, τ_y^*

Four values of τ_y^* are discussed: (p) $\tau_y^* = 1$ Pa, (q) $\tau_y^* = 3$ Pa, (s) $\tau_y^* = 4.8$ Pa (base case), and (t) $\tau_y^* = 6.4$ Pa. The yield stress induces the solid behavior of the material and the plastic phenomena.

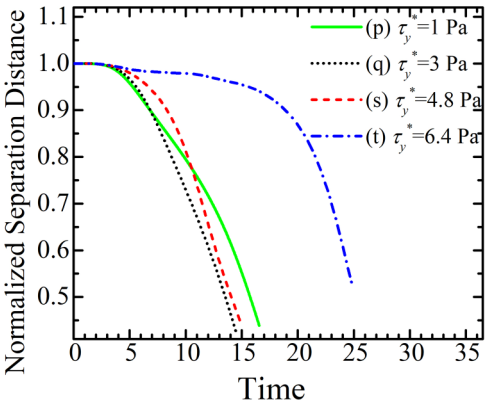

FIG. 21. Time evolution of normalized separation distance for the different values of yield stress.

It is also the reason that EVP materials behave elastically at low values of deformation, i.e., they exhibit elastoplasticity, in contrast to viscoelastic fluids that do not. The yield stress affects only Bn. So equivalently this is a parametric analysis on Bn. The corresponding Bn numbers are (p) 0.025, (q) 0.076, (s) 0.12, and (t) 0.163. We depict our results in terms of τ_y^*.

In Fig. 21 we observe that the approach times do not vary monotonically with increasing values of yield stress. In fact, the material with the smallest $\tau_y^* = 1$ Pa has a longer approach time than cases (q) and (s), but a smaller approach time compared to case (t), which has the highest Bn. Increasing the yield stress towards its critical value for bubble entrapment increases the solid behavior of the material and larger stresses are required to break its structure. The incubation period of case (p) is smaller than case (q). This is because the material is softer, and the faster merging of the yielded areas around the bubbles transmits to the TB the information that a LB is present in front of it quicker than in other cases and initiates the interaction earlier. However, the soft response of this material comes again into play soon after, when all areas around the bubbles have yielded and the response resembles more that in a viscoelastic fluid. With smaller deformation rates, elasticity is expressed weakly. Since there is decrease of elastoplasticity, which normally accelerates the approach as we saw earlier, the curve of case (p) moves beyond the curves of the two higher yield stress values. Regarding the large Bn case (t), it is chosen based on the entrapment conditions of a SB shown by Moschopoulos *et al.* [9]. The critical Bn_{cr} in their simulations using the same Carbopol 0.1% is calculated to be 0.16, for a limiting bubble radius of 0.003 m and a yield stress 4.71 Pa according to their fit. Case (t) with $\mathrm{Bn} = 0.163$ is slightly above this threshold where a single bubble should be trapped. However, our results show that the pair of bubbles approaches proving that interaction increases the Bn_{cr} for a pair. This agrees with the observations of Chaparian and Frigaard on multiple air inclusions in viscoplastic fluids [14].

In Fig. 22(p) we observe that the overshoot has disappeared so elastic phenomena have faded, although neither Ar nor Wi have changed. Both bubbles travel with velocities that are closer in value, and no effect from the confined space between them arises. As we raise the yield stress in case (q), the overshoot appears, so elastic phenomena are gradually becoming important, and a plateau follows in the curve of LB. The plateau is clearly visible also in cases (s) and (t).

In Fig. 23(p) large, yielded areas appear around the bubble pair. The material lacks elastoplasticity; this is revealed from the bubble shapes. As Fraggedakis *et al.* have shown [16], small bubbles in viscoelastic fluids create a weak flow field around them and induce a mild elastic response of the material. So bubbles acquire slightly extended spherical shapes. This is observed in case (p). The sizes of yielded areas decrease as we increase the yield stress or Bn equivalently.

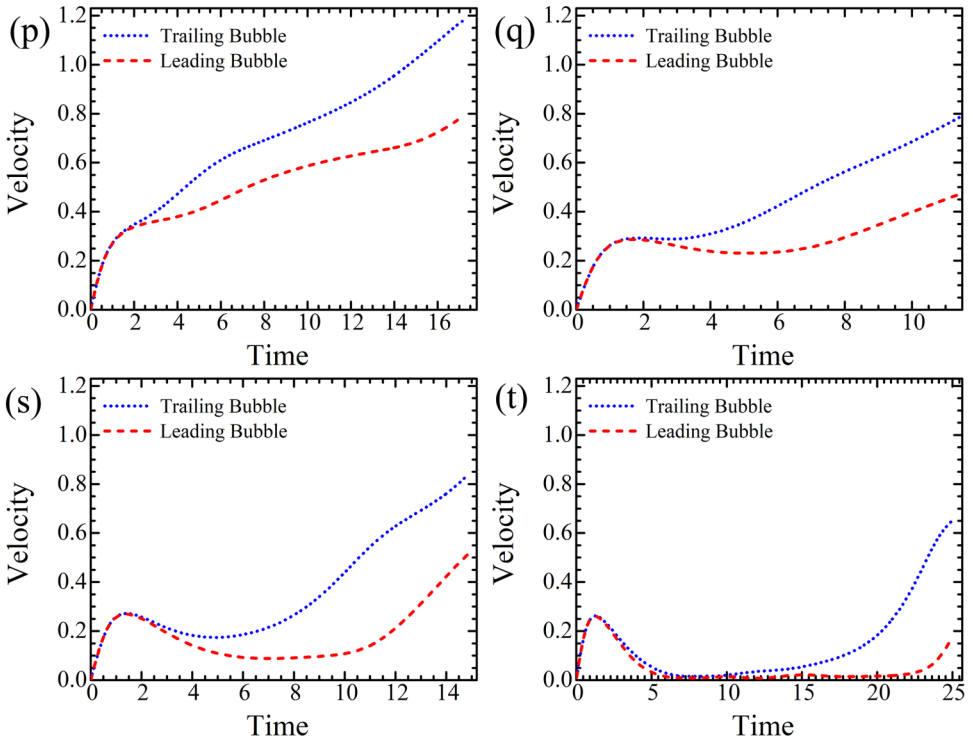

FIG. 22. Time evolution of velocities for (p) $\tau_y^* = 1$ Pa, (q) $\tau_y^* = 3$ Pa, (s) $\tau_y^* = 4.8$ Pa (base case), and (t) $\tau_y^* = 6.4$ Pa.

VI. SUMMARY AND CONCLUSIONS

We studied the interaction between two equal-sized, coaxially placed bubbles during their buoyancy-driven rise inside an EVP material using the SHB model [17]. We investigated the mechanism of interaction of small bubbles in the elastoplastic regime, with bubbles of 4 mm radius in an initial separation distance of 20 mm. We showed that a "bridge" of shear stresses develops in the space between them, extending from the leading bubble all the way back to the trailing bubble, which loads the material with stresses. The stored stresses "soften" the material bringing it closer to yielding conditions, which facilitates the flow and acceleration of the trailing bubble. At the same time tensile stresses develop at the rear pole of both bubbles deforming them. The open space behind the rear pole of the trailing bubble allows it to deform to an inverted teardrop shape, which is hydrodynamically favorable and adds to its acceleration. On the other hand, the space behind the leading bubble is confined by the trailing bubble deforming the LB to a prolate shape of higher resistance, leading to its lower velocity. Moreover, during the bubble approach shear and extension thinning contribute to the decrease of the resistance on the trailing bubble. Thus, the distance separating the bubbles decreases. When the bubbles are close enough, the sheltering effect, i.e., the pressure drop at the leading bubble's rear pole, draws the trailing bubble towards it. The LB is pushed by the TB and raises its velocity. Simulations are terminated when the thickness of the thin film at the axis of symmetry has decreased to 0.15.

Increasing the initial separation distance, we showed that the time of approach increases. Most importantly, however, irrespective of their initial separation, the bubbles always approach each other due to the storage of residual stresses in the material that remain in it indefinitely due to the hyperelastic nature of the solid. Varying the radius of the bubbles while also varying proportionally their initial separation distance, we studied the interplay between elastoplasticity and inertia. Small

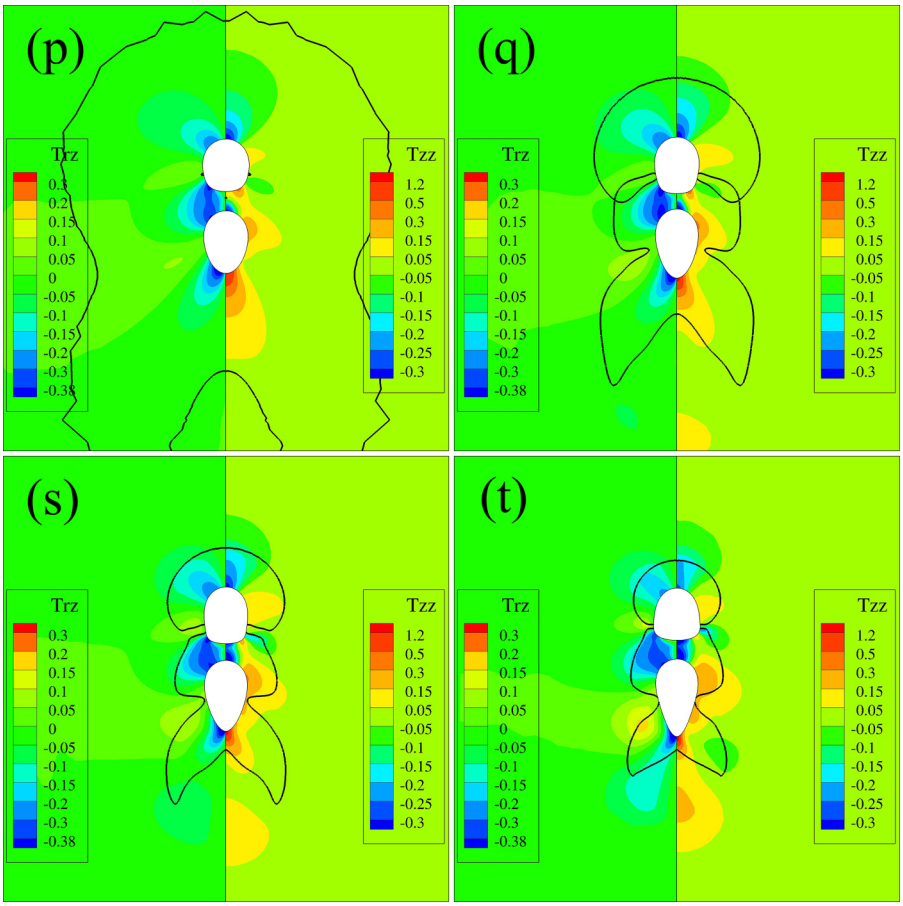

FIG. 23. Bubble shapes, shear stresses to the left, normal axial stresses to the right and yield surfaces indicated with solid black line at normalized separation distance 0.6 for (p) $\tau_y^* = 1$ Pa at time = 14.2, (q) $\tau_y^* = 3$ Pa at time = 12.04, (s) $\tau_y^* = 4.8$ Pa at time = 12.7 (base case), and (t) $\tau_y^* = 6.4$ Pa at time = 24.1.

bubble pairs exhibit increased elastoplasticity, and the largest approach time, despite their small initial separation distance. Bubbles of lower buoyancy require more time to start moving and eventually approach each other. Raising their size while still in the elastoplastic regime reduces the approach time as long as the bubble pair has enough driving force (buoyancy) to initiate motion. Raising the radius even further results in a transition from purely elastoplastic to a mixed elastoplastic-inertial regime where bubbles are initially deformed to inverted teardrop shapes, but soon after they become more oblate. Finally, the largest bubbles enter from the beginning the inertial regime and their shapes are oblate. Bubbles in the mixed elastoplastic-inertial regime need approximately the same approach time with the inertial ones, because the elastoplastic effects that contribute to closing the distance fade. At the same time, bubbles in the inertial regime have a more pronounced shear and extension thinning that aid in closing the separation distance faster despite its larger initial value.

Next, we studied the impact of material properties on the dynamics of the flow. Starting with elasticity, we predicted that the lower the value of the elastic modulus, the more hydrodynamically favorable the shapes become, which accelerates the approach. Changing the consistency index alters both the elastic and viscous response. Higher values of this property result in more elastic and more viscous materials. Promoting elasticity generally contributes to the approach, however the

viscous effects prevail. So increasing the value of the consistency index results in a slowdown of the whole process. A lower value of the shear thinning exponent results in a faster bubble approach. A very small value of the yield stress delays the approach, because the elastoplastic phenomena that promote it are suppressed. Raising the yield stress initially reduces the approach time because elastoplastic phenomena are reintroduced. Further increasing it delays their approach because bubbles need to generate higher stresses in the material to shatter its structure. Raising the yield stress even further results in entrapment of the bubble pair.

Our results contribute to an improved understanding of bubble interaction in non-Newtonian fluids, and in particular they open this discussion for yield stress materials with elasticity. The focus of the present study on equal-size bubbles shows that no bubble separation or even constant distance can arise for any value of the geometric parameters or material properties examined, due to the plethora of drag reducing mechanisms under the same driving force. So, in the presence of multiple bubbles inside an EVP material, clustering is expected to occur with bubbles attracting each other and, perhaps, initiating phase separation between the EVP material and the gaseous phase. We anticipate that this behavior can be applied to degassing yield stress materials. The latter could be achieved by following the counterintuitive operation of feeding the sample with gas bubbles to remove the already entrapped bubbles inside the material, without reducing the pressure. However, the flow rate should be carefully chosen according to the observations of Divoux *et al.* [30], who showed that the stable bubbling regime can be maintained up to a critical flow rate. Above it, a gas channel crossing the tank from bottom to top is formed, but this channel frequently collapses filling the material with small bubbles that get entrapped. Last but not least, the interest shifts to pairs of unequal tandem bubbles to investigate the full range of dynamic behaviors. Their different buoyancy could induce their separation or allow them to reach a steady distance. This sets the scope of our future study.

ACKNOWLEDGMENTS

This work was supported by the Hellenic Foundation of Research and Innovation, under Grant No. HFRI FM17-2309 MOFLOWMAT. D. Pettas participated in the preliminary stages of this research.

APPENDIX: FURTHER DETAILS ON MESH

1. Initial mesh generation

The initial mesh consists of a structured part around the bubbles and an unstructured part in the rest of the domain away from the bubbles. The geometry and mesh are constructed using the open-access software SALOME. We choose a structured mesh to have complete control over the areas in which it needs to be finer. The structured part, as seen in Fig. 24(a), is limited to an ellipse surrounding the bubbles. The major axis of the ellipse is chosen so that the distance from the center of volume of each bubble to the corresponding pole of the ellipse is 3.5. For example, the base case with initial separation distance 5, so the center of volume of LB is at $+2.5$ and the one of TB at -2.5, has a large radius for the ellipse equal to 6. The small radius of the ellipse in all cases is 4.5 times the bubble radius. In this way we ensure that the mesh is appropriate in all regions of interest and times. Each bubble interface is discretized in 1570 segments of equal length $\sim$0.002 to accurately carry out the surface integrations; see Figs. 24(b) and 24(c). Around each bubble there are seven zones in which we gradually increase the size of elements to maintain an acceptable computational time. The "fading" factor between two consecutive areas of discretization is 0.75, meaning that the opposite edge of each new refinement zone has 25% less nodes than the previous one. The intermediate space between bubbles is partitioned as seen in Fig. 24(a) to create quadrangles that allow the formation of the structured mesh. Finally, we split each quadrangle into two triangles. The unstructured part of the mesh is constructed using the NETGEN algorithm with minimum element size 0.1, maximum element size 30, and a growth rate parameter of 0.5. The typical mesh we used for simulations of the

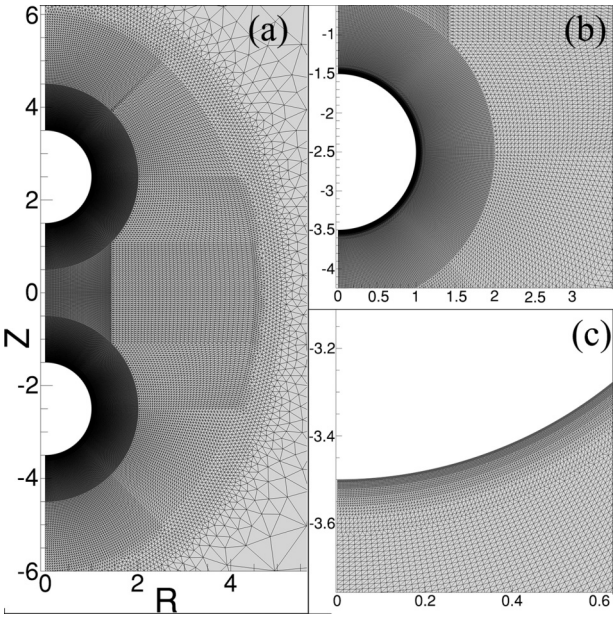

FIG. 24. Close-ups of a typical initial mesh (a) at a distance to show the ellipse of structured mesh, (b) close-up, around one bubble, and (c) close-up near the rear pole of the trailing bubble.

base case and all the parametric analysis cases, except the one of varying initial separation distance, has approximately 185 000 elements packed in the region of interest around the bubbles. As initial computational domain we used the initial one with the undeformed spherical bubbles.

2. Remeshing procedure

The free surfaces deform as dictated by the kinematic boundary condition; hence their nodes move, and the elements deform with time, following the arbitrary Lagrangian-Eulerian (ALE) methodology employed in this work. Additionally, the elliptic grid generation method mitigates the element deformation with an edge on the interface towards nearby elements in the bulk, so the deformation is spread in a region around the free surface nodes. This leads to a gradual skewness of the elements until code divergence occurs. The elliptic grid delays significantly the appearance of heavily skewed elements. However, the skewness of triangles is inevitable when bubbles exhibit large deformations (bubbles with high inertia where hat shapes are created). To remedy this problem the domain is remeshed.

This procedure takes place as follows: at each time step a criterion is examined. If the criterion is exceeded the simulation is paused, and the geometry at the last time step before pausing is recreated using the SALOME cad module. The geometry is then tessellated with the mesh generator provided by SALOME using the NETGEN algorithm, that produces an unstructured mesh. We maintain the initial number of nodes on the surface of each bubble. The necessary minimum and maximum element length arguments for NETGEN at each region are obtained by taking into account the undistorted element length from each area of the previous mesh. After the new mesh is formed, the solution from the old mesh with the old position of nodes is interpolated to the location of the new nodes for all field variables and the simulation continues.

Every time the remeshing criterion is exceeded, the old computational domain is discarded, and the physical domain at the first time step after remeshing becomes the new computational domain. In each remesh cycle, the total number of elements is not prespecified but depends on the current

TABLE III. Characteristics of the meshes used in the mesh convergence study.

Mesh	Element length on bubble surface	No. of triangular elements	No. of nodes	Time step
M1	0.007	60 386	29 560	0.03
M2	0.0035	103 095	50 516	0.015
M3	0.00175	208 682	102 529	0.0075

separation distance between bubbles. However, this number becomes progressively smaller after each remeshing since the bubbles approach and the space between them decreases.

3. Remeshing criterion

We examine all elements and define a ratio of each element area divided by the element area of the corresponding equilateral triangle inscribed in the same circumcircle:

$$f = \frac{A_{\text{elem}}}{A_{\text{eq}}}. \tag{A1}$$

This ratio is computed in each element separately and shows how close to an equilateral tringle the element in question is. Values closer to zero indicate a significantly deformed element. Knowing the positions of the nodes inside each element makes it easy to calculate the radius of the circumcircle and consequently the area of the equilateral triangle.

$$R = \frac{abc}{4A_{\text{elem}}}, \tag{A2}$$

where a, b, and c represent the lengths of each side of the triangle. Also, the area of the equilateral triangle with respect to the circumradius is calculated as

$$A_{\text{eq}} = \frac{3\sqrt{3}}{4}R^2. \tag{A3}$$

However, Eq. (A1) gives an absolute value and does not contain information on the initial state of each element. So we define its relative counterpart:

$$c = \frac{f - f_o}{f_o}, \tag{A4}$$

where f_o is the initial ratio. This definition has a positive value when an element is closer to the equilateral shape compared to its initial shape and a negative value when it becomes more stretched than initially. The threshold we set for our simulations is for $c < -0.8$, and it is checked at each time step. When the skewness of even one element surpasses the threshold, remeshing takes place.

4. Mesh convergence

We examine the mesh convergence of our numerical solutions by using three spatially and temporally refined meshes M1, M2, and M3, the characteristics of which are shown in Table III. Starting with M1, the meshes are consecutively doubled and the time step halved. For the mesh convergence test, we perform simulations until numerical divergence occurs skipping the remeshing cycles.

Figure 25(a) shows the variation of a very sensitive variable, τ_{zz}, on the axis of symmetry at time $t = 7.2$ for the base case, using M1–M3 meshes. Clearly the solution is mesh independent. In Fig. 25(b), we plot the effect of mesh size on another very sensitive variable, the yield surfaces at time 7.2. The same mesh independence holds for the yield surfaces around and near the bubbles.

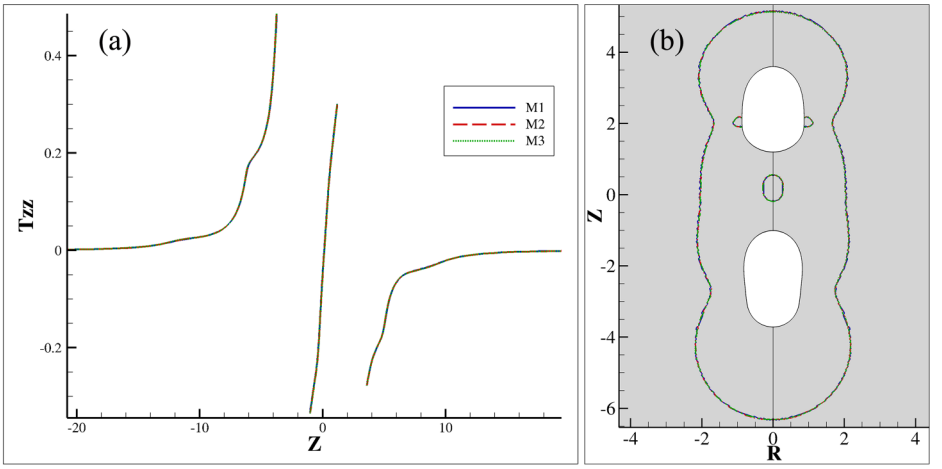

FIG. 25. Mesh convergence results of the base case at time = 7.2 (a) τ_{zz} along the axis of symmetry, the gaps correspond to the space occupied by the bubbles, and (b) yield surface ($|\tau_d| = \mathrm{Bn}$).

5. Form of the yield surface: Case (k)

We discuss the two "types" of wavy shapes of the yield surface in Fig. 11(k). The first type is in the rear of the umbrella-like shape around the leading bubble. This shape depends directly on this stress field and is in a finely discretized area. Therefore, this part of the yield surface has been determined with the same accuracy as the stresses and is real. The second type of wavy shapes is seen at the lowest part of Fig. 11(k). This arises because of the linear interpolation of the stresses and the larger size of the elements in this area compared to that in the vicinity of bubbles. We show in Fig. 26(a) the yield surface superimposed to the mesh at the same scale as Fig. 11(k). In Fig. 26(b) we depict a magnification of the wavy part of the yield surface. Clearly the corrugated part of the yield surface follows the local structure of these larger elements. This wavy shape type is also seen in the yield surface of Fig. 24(p).

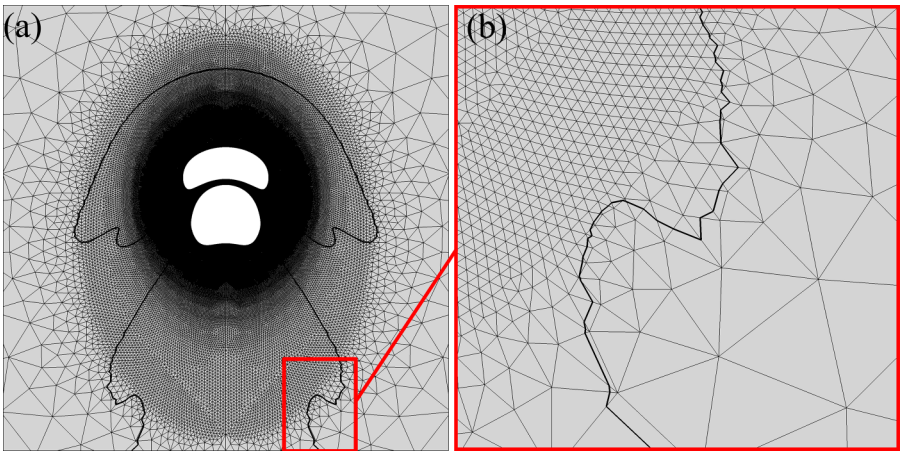

FIG. 26. Yield surface superimposed to the mesh for (a) the initial scale of Fig. 11(k) and (b) close-up of the region where the line becomes corrugated.

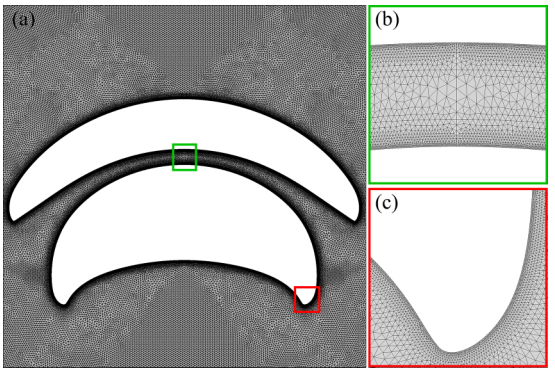

FIG. 27. Mesh of the domain for case (n): (a) snapshot containing both bubbles, (b) zoomed area of the snapshot in the middle of the film, and (c) zoomed area of the snapshot at the corner of the TB.

6. Large free surface deformation

We show the mesh formed around the bubbles for case (n). This case produces the stiffest conditions in terms of mesh distortion due to the extreme deformation of the free surface along with the translation of the bubbles squeezing the elements in the intermediate space between them. In Fig. 27 we show the mesh at the time instant of the results we showed earlier. As we can see in Fig. 27(b) the two bubbles approach and the elements of the initially dense intermediate space decrease.

[1] D. Izidoro, M. R. Sierakowski, N. Waszczynskyj, C. W. I. Haminiuk, and A. D. P. Scheer, Sensory evaluation and rheological behavior of commercial mayonnaise, Int. J. Food Eng. **3**, 1 (2007).
[2] A. F. Silva, T. A. Wood, D. J. M. Hodgson, J. R. Royer, J. H. J. Thijssen, A. Lips, and W. C. K. Poon, Rheological design of thickened alcohol-based hand rubs, Rheol. Acta **61**, 571 (2022).
[3] C. J. Dimitriou and G. H. McKinley, A comprehensive constitutive law for waxy crude oil: A thixotropic yield stress fluid, Soft Matter **10**, 6619 (2014).
[4] W. Mbasha, I. Masalova, R. Haldenwang, and A. Malkin, The yield stress of cement pastes as obtained by different rheological approaches, Appl. Rheol. **25**, 53517 (2015).
[5] J. Tsamopoulos, Y. Dimakopoulos, N. Chatzidai, G. Karapetsas, and M. Pavlidis, Steady bubble rise and deformation in Newtonian and viscoplastic fluids and conditions for bubble entrapment, J. Fluid Mech. **601**, 123 (2008).
[6] Y. Dimakopoulos, M. Pavlidis, and J. Tsamopoulos, Steady bubble rise in Herschel-Bulkley fluids and comparison of predictions via the Augmented Lagrangian Method with those via the Papanastasiou model, J. Non-Newton. Fluid Mech. **200**, 34 (2013).
[7] M. K. Tripathi, K. C. Sahu, G. Karapetsas, and O. K. Matar, Bubble rise dynamics in a viscoplastic material, J. Non-Newton. Fluid Mech. **222**, 217 (2015).
[8] A. Kordalis, S. Varchanis, G. Ioannou, Y. Dimakopoulos, and J. Tsamopoulos, Investigation of the extensional properties of elasto-visco-plastic materials in cross-slot geometries, J. Non-Newton. Fluid Mech. **296**, 104627 (2021).
[9] P. Moschopoulos, A. Spyridakis, S. Varchanis, Y. Dimakopoulos, and J. Tsamopoulos, The concept of elasto-visco-plasticity and its application to a bubble rising in yield stress fluids, J. Non-Newton. Fluid Mech. **297**, 104670 (2021).
[10] W. F. Lopez, M. F. Naccache, and P. R. de Souza Mendes, Rising bubbles in yield stress materials, J. Rheol. **62**, 209 (2018).

[11] A. Pourzahedi, M. Zare, and I. A. Frigaard, Eliminating injection and memory effects in bubble rise experiments within yield stress fluids, J. Non-Newton. Fluid Mech. **292**, 104531 (2021).
[12] J. Zhang, M. J. Ni, and J. Magnaudet, Three-dimensional dynamics of a pair of deformable bubbles rising initially in line. Part 1. Moderately inertial regimes, J. Fluid Mech. **920**, A16 (2021).
[13] J. R. Vélez-Cordero, D. Sámano, P. Yue, J. J. Feng, and R. Zenit, Hydrodynamic interaction between a pair of bubbles ascending in shear-thinning inelastic fluids, J. Non-Newton. Fluid Mech. **166**, 118 (2011).
[14] E. Chaparian and I. A. Frigaard, Clouds of bubbles in a viscoplastic fluid, J. Fluid Mech. **927**, R3 (2021).
[15] W. Yuan, M. Zhang, B. C. Khoo, and N. Phan-Thien, Hydrodynamic interaction and coalescence of two inline bubbles rising in a viscoelastic liquid, Phys. Fluids **33**, 083102 (2021).
[16] D. Fraggedakis, M. Pavlidis, Y. Dimakopoulos, and J. Tsamopoulos, On the velocity discontinuity at a critical volume of a bubble rising in a viscoelastic fluid, J. Fluid Mech. **789**, 310 (2016).
[17] P. Saramito, A new elastoviscoplastic model based on the Herschel-Bulkley viscoplastic model, J. Non-Newton. Fluid Mech. **158**, 154 (2009).
[18] S. Varchanis, A. Syrakos, Y. Dimakopoulos, and J. Tsamopoulos, A new finite element formulation for viscoelastic flows: Circumventing simultaneously the LBB condition and the high-Weissenberg number problem, J. Non-Newton. Fluid Mech. **267**, 78 (2019).
[19] S. Varchanis, A. Syrakos, Y. Dimakopoulos, and J. Tsamopoulos, PEGAFEM-V: A new Petrov-Galerkin finite element method for free surface viscoelastic flows, J. Non-Newton. Fluid Mech. **284**, 104365 (2020).
[20] T. J. R. Hughes, L. P. Franca, and M. Balestra, A new finite element formulation for computational fluid dynamics: V. Circumventing the Babuška-Brezzi condition: A stable Petrov-Galerkin formulation of the Stokes problem accommodating equal-order interpolations, Comput. Methods Appl. Mech. Eng. **59**, 85 (1986).
[21] R. Guénette and M. Fortin, A new mixed finite element method for computing viscoelastic flows, J. Non-Newton. Fluid Mech. **60**, 27 (1995).
[22] A. N. Brooks and T. J. R. Hughes, Streamline upwind/Petrov-Galerkin formulations for convection dominated flows with particular emphasis on the incompressible Navier-Stokes equations, Comput. Methods Appl. Mech. Eng. **32**, 199 (1982).
[23] S. Varchanis, D. Pettas, Y. Dimakopoulos, and J. Tsamopoulos, Origin of the Sharkskin Instability: Nonlinear Dynamics, Phys. Rev. Lett. **127**, 088001 (2021).
[24] S. Varchanis, S. J. Haward, C. C. Hopkins, A. Syrakos, A. Q. Shen, Y. Dimakopoulos, and J. Tsamopoulos, Transition between solid and liquid state of yield-stress fluids under purely extensional deformations, Proc. Natl. Acad. Sci. USA **117**, 12611 (2020).
[25] Y. Dimakopoulos and J. Tsamopoulos, A quasi-elliptic transformation for moving boundary problems with large anisotropic deformations, J. Comput. Phys. **192**, 494 (2003).
[26] N. Chatzidai, A. Giannousakis, Y. Dimakopoulos, and J. Tsamopoulos, On the elliptic mesh generation in domains containing multiple inclusions and undergoing large deformations, J. Comput. Phys. **228**, 1980 (2009).
[27] A. Syrakos, Y. Dimakopoulos, and J. Tsamopoulos, A finite volume method for the simulation of elastoviscoplastic flows and its application to the lid-driven cavity case, J. Non-Newton. Fluid Mech. **275**, 104216 (2020).
[28] D. Bhaga and M. E. Weber, In-line interaction of a pair of bubbles in a viscous liquid, Chem. Eng. Sci. **35**, 2467 (1980).
[29] Z. Tian, X. Li, Y. Cheng, and L. Wang, Interaction of two in-line bubbles of equal size rising in viscous liquid, Chinese J. Chem. Eng. **28**, 54 (2020).
[30] T. Divoux, E. Bertin, V. Vidal, and J. C. Géminard, Intermittent outgassing through a non-Newtonian fluid, Phys. Rev. E **79**, 056204 (2009).